VILNIUS UNIVERSITY

DARIUS DOBROVOLSKAS

STUDY OF CARRIER DYNAMICS IN InGaN USING SPATIALLY-RESOLVED PHOTOLUMINESCENCE TECHNIQUES

Doctoral thesis

Physical Sciences, Physics (02 P), Semiconductor Physics (P 265)

Vilnius, 2013

The research work has been carried out in 2009-2013 at the Semiconductor Physics Department and the Institute of Applied Research, Vilnius University.

Scientific supervisor:

Prof. habil. dr. Gintautas Tamulaitis (Vilnius University, Physical Sciences, Physics – 02 P, Semiconductor physics – P 265).

VILNIAUS UNIVERSITETAS

DARIUS DOBROVOLSKAS

KRŪVININKŲ DINAMIKOS InGaN TYRIMAS LIUMINESCENCIJOS SU ERDVINE SKYRA METODAIS

Daktaro disertacija

Fiziniai mokslai, fizika (02 P), puslaidininkių fizika (P 265)

Vilnius, 2013

Disertacija rengta 2009 – 2013 metais Vilniaus universitete, Puslaidininkių fizikos katedroje ir Taikomųjų mokslų institute.

Mokslinis vadovas:

Prof. habil. dr. Gintautas Tamulaitis (Vilniaus universitetas, fiziniai mokslai, fizika –02 P, puslaininkių fizika – P 265)

Reziumė

Intensyvūs III-grupės nitrindinių puslaidininkių tyrimai, atlikti per pastaruosius du dešimtečius, leido pasiekti didelę pažangą šių puslaidininkių ir darinių auginimo bei panaudojimo optoelektroninių ir elektroninių prietaisų gamybos srityse. Augantis baltą šviesą skleidžiančių šviestukų (šviesos diodų) poreikis bendrajam apšvietimui yra pagrindinis šių plačiatarpių puslaidininkių tobulinimo variklis. Šviestukai yra energiją taupantys šviesos šaltiniai, suteikiantys papildomų funkcionalumo ir dizaino galimybių. Prognozuojama, kad InGaN pagrindu veikiantys šviestukai galiausiai pakeis įprastines kaitrines ir flourescencines lempas.

Mėlyną šviesą skleidžiantys InGaN šviestukai jau yra sėkmingai komercializuoti. Norint, kad šviestukai skleistų didesnio bangos ilgio (žalią, raudoną) šviesą, indžio kiekį aktyviojoje šviestuko srityje būtina padidinti. Tačiau tai yra gan sudėtinga. Didinant indžio kiekį, InGaN šviestukų našumas sparčiai mažėja. Kadangi kitų puslaidininkių, tinkamų šviestukams šioje spektro dalyje, nėra, ši spektrinė dalis net praminta „žaliuoju mirties slėniu“.

InGaN šviestukų aktyviosios sritys dažniausiai yra auginamos ant safyro padėklų. Tačiau dėl InGaN ir padėklo gardelių neatitikimo šių medžiagų sandūroje atsiranda defektai, kurie blogina prietaisų parametrus. Siūlinių dislokacijų tankis InGaN yra net keliomis eilėmis didesnis nei kituose III-V grupės puslaidininkiuose, kurie jau naudojami optoelektronikoje. Nepaisant to, InGaN šviestukai yra pakankamai našūs, kad galėtų konkuruoti su kitais šviesos šaltiniais. Toks InGaN atsparumas defektams yra neabejotinas šios medžiagos privalumas, bet jis nėra gerai suprastas. Manoma, kad InGaN junginio sudėties fliuktuacijos sukuria potencialo fliuktuacijas, kuriose lokalizuojami nepusiausvyrieji krūvininkai. Tokiu būdu lokalizuotiems krūvininkams tikimybė patekti į nespindulinės rekombinacijos centrus sumažėja. Ši ir kitos InGaN puslaidininkio ypatybės priklauso nuo indžio kiekio InGaN junginyje. Todėl tolimesniam InGaN šviestukų tobulinimui yra svarbu tirti netolygiai pasiskirčiusios liuminescencijos prigimtį ir ypatumus.

Šis darbas yra skirtas krūvininkų lokalizacijos ir rekombinacijos tyrimams InGaN epitaksiniuose sluoksniuose ir dariniuose panaudojant fotoliuminescencinę spektroskopiją submikrometrine erdvine skyra. Tyrimas buvo atliekamas konfokaliniu ir skenuojančiuoju artimojo lauko optiniu mikroskopu. Optinius bandinių tyrimus papildė struktūrinė analizė. Tai leido išsamiau charakterizuoti InGaN junginio ypatumus.

Tiriant InGaN epitaksinius sluoksnius, buvo nagrinėjama gardelės įtempimo ir jos relaksacijos poveikis optinėms InGaN savybėms. Pastebėti fotoliuminescencijos spektro parametrų kitimai susieti su sluoksnio struktūriniais pokyčiais.

Iškaitinimo daroma įtaka tirta InGaN epitaksiniuose sluoksniuose ir daugialakščiuose kvantiniuose dariniuose. Pademonstruota, kad priemaišinės kilmės liuminescenciją InGaN sluoksnyje įmanoma nuslopinti sluoksnius iškaitinant lazerio spinduliuote. Be to parodyta, kad netyčinis daugialakščių kvantinių InGaN darinių iškaitinimas vyksta jau auginimo metu, formuojant *p* tipo sluoksnius.

Ištirta neigiama koreliacija tarp fotoliuminescencijos intensyvumo ir juostos smailės bangos ilgio InGaN daugialakščiuose kvantiniuose dariniuose su dideliu indžio kiekiu. Pasiūlyta tokį nebūdingą InGaN junginiui fotoliuminescencijos pasiskirstymą paaiškiti netolygiu nespindulinių centrų pasiskirstimu.

Daugialakščiuose InGaN kvantiniuose dariniuose lokaliai stebėtas liuminescencijos intensyvumo padidėjimas dėl sąveikos su lokalizuotais paviršiniais plazmonais, indukuotais sidabro nanodalelėse. Parodytas potencialo fliuktuacijų daromas poveikis rezonansinei sąveikai tarp optinių dipolių kvantiniuose dariniuose ir lokalizuotų paviršinių plazmonų, indukuotų sidabro nanodalelėse.

Acknowledgments

I would like to gratefully acknowledge the enthusiastic supervision of prof. Gintautas Tamulaitis during this work.
Also I thank prof. Artūras Žukauskas and prof. Saulius Juršėnas for the possibility to carry out this research at the Institute of Applied Research.
I thank dr. Jūras Mickevičius for valuable discussions and advice. I would like to thank all my friends and colleagues for help and friendly work atmosphere at the Institute.
I would like to express my heartfelt thanks to my family and wife for their constant support and encouragement through the duration of my studies.

This work has been supported by the Research Council of Lithuania and the Lithuanian State Science and Study Foundation.

Table of Contents

List of abbreviations

AFM	atomic force microscopy
AES	Auger electron spectroscopy
CW	continuous wave
CoM	center of mass
FWHM	full width at half maximum
LED	light emitting diode
LSP	localized surface plasmon
MOCVD	metalorganic chemical vapor deposition
MQWs	multiple quantum wells
NPs	nanoparticles
Nd:YAG	neodymium-doped yttrium aluminum garnet
PL	photoluminescence
QCSE	quantum confined Stark effect
SNOM	scanning near-field optical microscopy
XRD	X-ray diffraction

1. Introduction

Over the past two decades, an extensive investigation of group-III nitrides has resulted in a significant progress in growth and processing technologies of these semiconductors. Such rapid development is fueled, in particular, by the growing demand and expectations in white light emitting diodes (LEDs) for solid state lighting. LEDs are energy-efficient and provide additional functionalities and design options in lighting. It is expected that InGaN-based white LEDs will ultimately replace the conventional incandescent light bulbs and fluorescent lamps. InGaN semiconductor alloy is potentially suitable for light emission in the entire visible range. InGaN-based LEDs have already penetrated into medical, signage, display, and automotive applications.

Blue emitting InGaN-based LEDs are already successfully commercialized. For LEDs to emit at longer wavelengths (green and red), incorporation of higher indium content in the active layer is needed. However, this turned out to be challenging. At higher indium contents, the quantum efficiency of InGaN-based LEDs rapidly drops to an unacceptably low level. Since there are no other materials for efficient LEDs emitting in this region, the region has been nicknamed as the “green valley of death”. Several effects have been suggested to explain the origin of this low efficiency: the influence of defects, polarization effects, compositional inhomogeneities, etc.

Currently, InGaN LEDs are grown on lattice-mismatched substrates, predominantly on sapphire. This heteroepitaxial growth creates a large dislocation density. In fact, the threading dislocation density in InGaN is still many orders of magnitude higher than in other III-V semiconductors used in electronics and optoelectronics. Despite that, InGaN-based LEDs are efficient enough to compete with conventional light sources in many applications. Certainly, the insensitivity of optical properties on dislocation density is an advantage of InGaN, but understanding of this phenomenon is still incomplete. It is suggested, that the carrier localization by compositional inhomogeneities in InGaN enhances electron-hole wavefunction overlap and, subsequently,

enhances radiative recombination. At the same time, the localization prevents carriers from reaching nonradiative recombination centers and recombining there nonradiatively. Moreover, inhomogeneous distribution of the luminescence intensity is typically observed in InGaN samples. However, up to now, the spatial dimensions of these fluctuations are unclear. On the other hand, group III nitrides exhibit strong internal electric field due to piezoelectric and spontaneous polarization. The field separates electron and hole wavefunctions in quantum wells, thus reducing the efficiency of radiative recombination. Inhomogeneous field distribution might also contribute to spatial variation of luminescence intensity. Thus, the study of spatial inhomogeneity of luminescence in InGaN provides an insight into carrier localization and recombination peculiarities and is important for the development of LEDs.

The experimental work in this thesis is based on optical characterization by spatially-resolved photoluminescence techniques, namely confocal and scanning near-field optical microscopy. Combination of these techniques with the structural analysis provides a deeper insight into peculiarities of InGaN.

Main goal

The thesis is aimed at gaining new knowledge on carrier localization and recombination in InGaN epilayers and structures by using photoluminescence spectroscopy with sub-micrometer spatial resolution.

Main objectives

- To investigate the influence of lattice strain and its relaxation on the in-plane inhomogeneities of optical properties in InGaN epilayers and reveal the correlation between optical properties and peculiarities in crystal structure.

- To study the influence of thermal annealing on optical properties of InGaN epilayers and MQWs, to explore the feasibility of laser annealing for suppression of defect-related emission in InGaN epilayers, and to reveal the influence of unintentional annealing at elevated temperatures during fabrication of InGaN structures.
- To investigate the origin of negative correlation between photoluminescence intensity and band peak wavelength in InGaN MQWs with high indium content.
- To study the emission enhancement in the vicinity of metal nanoparticles due to coupling of optical dipoles in InGaN MQWs with the localized surface plasmons in the nanoparticles.

Novelty and importance

The influence of the lattice strain relaxation on spatial PL intensity distribution was demonstrated. A new source of inhomogeneous PL distribution caused by nanocolumn-like structures in strain-relaxed InGaN epilayers is revealed.

Feasibility of suppressing the defect-related emission in InGaN epilayers by laser annealing is verified by optical and structural characterization.

Unintentional thermal annealing during overgrowth of *p*-type layer in InGaN MQW structures is revealed.

A novel interpretation for negative correlation between PL intensity and band peak wavelength in high-indium-content InGaN MQWs is suggested.

The influence of potential fluctuations in InGaN MQWs on PL intensity enhancement via optical dipole coupling with localized surface plasmons is demonstrated.

Statements to defend

1. The formation of the relaxed sublayer at increasing InGaN epilayer thickness results in a double peaked photoluminescence spectra. The further growth results in the formation of the nanocolumn-like structures having a relaxed lattice, indium content as in the initial strained sublayer and a lower density of nonradiative recombination centers.

2. In InGaN LED structures, the overgrowth of *p*-type layer at elevated temperature results in unintentional thermal annealing. The influence of the quantum confined Stark effect on emission properties is large in thin *p*-type layers but saturates and is gradually overwhelmed by the stronger influence of the thermal annealing.

3. The negative correlation between photoluminescence intensity and peak wavelength can be explained by inhomogeneous defect distribution. Since the carriers occupying the states with smaller localization energy have a larger probability to delocalize and recombine nonradiatively, the luminescence band is redshifted in areas with higher defect density, i.e. the areas exhibiting lower photoluminescence intensity.

4. The enhancement of luminescence intensity due to coupling of optical dipoles in InGaN/GaN quantum wells with localized surface plasmons in isolated silver nanoparticles is strongly influenced by the potential fluctuations. The enhancement is stronger in the areas that emit light at wavelengths that match better the localized surface plasmon resonance.

Layout of the thesis

The thesis consists of seven chapters divided into sections. An introduction, a list of publications, main goal and objectives, novelty, and statements to defend are presented in the first chapter.

A brief general overview of structural, optical and electronic properties of InGaN is presented in chapter 2. An emphasis is made on growth issues and spatial inhomogeneity of photoluminescence properties of InGaN.

In chapter 3, the techniques for spatially-resolved photoluminescence study and experimental setups used for characterization of the samples are described.

The original results of the thesis are presented in chapters 4-7. Each of these chapters starts with a review section reviewing the existing knowledge on the subject under study in the chapter, problems and specific objectives of the original research, the results of which are described in the subsequent sections of the chapter. The main results in each of these chapters are concluded in a summary.

In Chapter 4, the results on the influence of strain and its relaxation on photoluminescence properties of InGaN are discussed. Spatial PL distribution in a series of InGaN epilayers of different indium content is compared. It is shown that nanocolumn-like structures on the surface of the relaxed layer contribute to additional in-plane PL inhomogeneities.

In Chapter 5, the results on the study on InGaN thermal annealing are presented. The study is divided into two parts. In the first part of the chapter, In-rich InGaN epilayers exhibiting a strong defect related luminescence are discussed. A possibility to suppress the defect-related emission by laser annealing is demonstrated and laser-annealing-induced compositional changes in InGaN epilayers are described. The second part of the chapter focuses on the influence of elevated temperature during the growth of the InGaN/GaN MQWs structures. The concurrent influences of thermal annealing and strain on PL properties are discussed.

In chapter 6, spatial distribution of photoluminescence in LED structures with InGaN multiple quantum wells as an active region is studied. A negative correlation between PL intensity and band peak wavelength is observed. The origin of the observed optical features are discussed, the discussion is supported by model calculations.

In chapter 7, emission efficiency enhancement in InGaN quantum wells due to coupling of the optical dipole with localized surface plasmons in Ag nanoparticles is investigated. The influence of potential fluctuations on the coupling with localized surface plasmons is revealed.

The concluding summary is presented at the end of the thesis.

Author's contribution

All of the measurements by confocal microscope, scanning near field microscope, and atomic force microscope were performed by the author. X-ray diffraction reciprocal space mappings were performed at AIXTRON SE, Herzogenrath, Germany. The Auger spectrometry measurements were performed by J. Miškinis and dr. V. Kazlauskienė at the Materials Science Laboratory, Vilnius University. The measurements of spatially-integrated PL under quasi-steady-state excitation have been carried out by dr. J. Mickevičius. Most of the analysis of the data was done by the author. The statistical analysis of PL mapping images discussed in section 5.3.2 was performed by dr. J. Mickevičius. The interpretation was discussed with scientific supervisor prof. G. Tamulaitis. The author has prepared drafts and, after discussions with co-authors, the final versions for 6 out of 7 papers related with the thesis.

List of publications

List of publications related to the thesis

P1. **D. Dobrovolskas**, J. Mickevičius, G. Tamulaitis, H.S. Chen, C.P. Chen, Y.L. Jung, Y.W. Kiang, C.C. Yang, Spatially resolved study of InGaN photoluminescence enhancement by single Ag nanoparticles, J. Phys. D: Appl. Phys. **46**, 145105 (2013)

P2. **D. Dobrovolskas**, A. Vaitkevičius, J. Mickevičius, Ö. Tuna, C. Giesen, M. Heuken, G. Tamulaitis, Correlation between structure and photoluminescence properties in InGaN epilayers with thickness below and above critical thickness, J. Appl. Phys. (2013) (*accepted*)

P3. J. Mickevičius, **D. Dobrovolskas**, I. Šimonytė, G. Tamulaitis, C.-Y. Chen, C.-H. Liao, H.-S. Chen, C.C. Yang, Unintentional annealing of the active layer in the growth of InGaN/GaN quantum well light-emitting diode structures, Phys. Stat. Solidi A **210**, 1657 (2013)

P4. G. Tamulaitis, **D. Dobrovolskas**, J. Mickevičius, V. Kazlauskienė, J. Miškinis, E. Kuokštis, P. Onufrijevs, A. Medvids, J.-J. Huang, C.-Y. Chen, C.-H. Liao, and C.C. Yang, Suppression of defect-related luminescence in laser-annealed InGaN epilayers, Phys. Stat. Solidi C **9**, 1021 (2012)

P5. **D. Dobrovolskas**, J. Mickevičius, E. Kuokštis, G. Tamulaitis, M. Shur, M. Shatalov, J. Yang, R. Gaska, Confocal spectroscopy of InGaN LED structures, Journal of Physics D-Applied Physics, **44**, 135104 (2011)

P6. **D. Dobrovolskas**, J. Mickevičius, V. Kazlauskienė, J. Miškinis, E. Kuokštis, G. Tamulaitis, P. Onufrijevs, A. Medvids, J.J. Huang, C.Y. Chen, C.H. Liao, C.C. Yang, Influence of laser annealing on defect-related luminescence of InGaN epilayers, Journal of Luminescence, **131,** 1322 (2011)

P7. G. Tamulaitis, J. Mickevičius, **D. Dobrovolskas**, E. Kuokštis, M. Shur, M. Shatalov, J. Yang, R. Gaska, Spatially-resolved photoluminescence study of high indium content InGaN LED structures, Phys. Status Solidi C 7, No. 7–8, 1869 (2010)

List of publications not related to the thesis

P8. E. Gaubas, I. Brytavskyi, T. Čeponis, **D. Dobrovolskas**, S. Juršėnas, J. Kusakovskij, V. Smyntyna, G. Tamulaitis, A. Tekorius, V. Borschak, Non-radiative and radiative recombination in CdS polycrystalline structures, Advances in Condensed Matter Physics, (2013) *(accepted*)

P9. K. Kazlauskas, A. Miasojedovas, **D. Dobrovolskas**, E. Arbačiauskaitė, V. Getautis, A. Šačkus, S. Juršėnas, Self-assembled nanoparticles of *p*-phenylenediacetonitrile derivatives with fluorescencce turn-on, J. Nanopart. Res. **14,** 877 (2012)

P10. G. Tamulaitis, J. Mickevičius, **D. Dobrovolskas**, E. Kuokštis, M.S. Shur, M. Shatalov, J. Yang, and R. Gaska, Carrier dynamics and efficiency droop in AlGaN epilayers with different Al content, Phys. Stat. Solidi C **9**, 1677 (2012)

P11. E. Jelmakas, M. Alsys, P. Gečys, **D. Dobrovolskas**, A. Kadys, G. Račiukaitis, R. Tomašiūnas, uGaN growth on laser patterned sapphire substrate: quality feature, Phys. Stat. Solidi C, **12**, 2448 (2012)

P12. **D. Dobrovolskas**, J. Mickevičius, G. Tamulaitis, V. Reipa, Photoluminescence of Si nanocrystals under selective excitation, Journal of Physics and Chemistry of Solids, **70**, 439-443 (2009)

List of conference presentations related to the thesis

C1. **D. Dobrovolskas,** E. Kuokštis, J. Mickevičius, G. Tamulaitis, Jeng-Jie Huang, Chih-Yen Chen, C. C. Yang, „*Epitaksinio InGaN sluoksnio su dideliu In kiekiu fotoliuminescencijos tyrimas konfokalinės spektroskopijos metodu*“, 38-oji Lietuvos nacionalinė fizikos konferencija, balandžio 8–10 d. 2009 m., Vilnius, Programa ir pranešimų tezės, p. 94 (poster presentation).

C2. **D. Dobrovolskas**, E. Kuokštis, J. Mickevičius, G. Tamulaitis, J.-J. Huang, C.-Y Chen, C.-C. Yang, “*Characterization of In-rich InGaN epitaxial layer using confocal spectroscopy*“, Book of Abstracts of the 11-th International Summer School-Conference Advanced Materials and Technologies, 27–31 August 2009, Palanga, p. 69 (poster presentation).

C3. G. Tamulaitis, J. Mickevičius, **D. Dobrovolskas**, E. Kuokštis, M. Shur, M. Shatalov, J. Yang, R. Gaska, “*Spatially-resolved Photoluminescence Study of High Indium Content InGaN LED Structures*“, The 8th International Conference on Nitride Semiconductors, 18–23 October 2009, ICC Jeju, Korea, Abstract book, Volume 1, p. 357-358 (poster presentation).

C4. **D. Dobrovolskas**, J. Mickevičius, E. Kuokštis, G. Tamulaitis, M. Shur, M. Shatalov, J. Yang, R. Gaska, “*Spatially and spectrally resolved photoluminescence study of InGaN LED structures*“, XXXIX „Jeszowiec“ 2010 International School and Conference on the Physics of Semiconductors, 19–24 June, Krynica-Zdroj, Poland, Abstract book, p. 149 (poster presentation).

C5. G. Tamulaitis, **D. Dobrovolskas**, J. Mickevičius, V. Kazlauskienė, J. Miškinis, E. Kuokštis, P. Onufrijevs, A. Medvids, J.J. Huang, C.Y. Chen, C.H. Liao, C.C. Yang, "*Suppression of defect-related luminescence in laser-annealed InGaN epilayers*", E-MRS 2011 Spring Meeting IUMRS ICAM 2011 & E-MRS / MRS Bilateral Conference on Energy May 9–13, 2011, Nice, France (poster presentation).

C6. G. Tamulaitis, J. Mickevičius, **D. Dobrovolskas**, E. Kuokštis, M.S. Shur, M. Shatalov, J. Yang, R. Gaska, "*Carrier dynamics and efficiency droop in AlGaN epilayers with different Al content*", Program and Abstracts of the 16th Semiconducting and Insulating Materials Conference (SIMC XVI), June 19–23, 2011, KTH, Stockholm, Sweden, p. We2-3 (oral presentation).

C7. **D. Dobrovolskas**, E. Kuokštis, J. Mickevičius, G. Tamulaitis, S. Suikhonen, "*Photoluminescence intensity spatial distribution dependence on well width in InGaN single quantum well*", Book of Abstracts of the 13-th International Summer School-Conference Advanced Materials and Technologies, 27-31 August 2011, Palanga, p.78 (poster presentation).

C8. **D. Dobrovolskas**, E. Kuokštis, J. Mickevičius, G. Tamulaitis, S. Suihkonen, „*Erdvinis fotoliuminescencijos intensyvumo pasiskirstymas InGaN vienalypiuose kvantiniuose lakštuose*", 39-oji Lietuvos nacionalinė fizikos konferencija, spalio 6-8 d. 2011 m., Vilnius, Programa ir pranešimų tezės, p. 64 (poster presentation)

C9. G. Tamulaitis, **D. Dobrovolskas**, J. Mickevičius, C.-W. Huang, C.-Y. Chen, C.-H. Liao, C. Hsieh, Y.-L. Jung, D.-M. Yeh, C.C. Yang, "*Spatially resolved study of surface-plasmon-enhanced photoluminescence in InGaN quantum wells*", Program of the E-MRS Spring Meeting, May 14-18, 2012, Strasbourg, France, p. T-13. (oral presentation).

C10. **D. Dobrovolskas**, G. Tamulaitis, J. Mickevičius, V. Kazlauskienė, J. Miškinis, E. Kuokštis, P. Onufrijevs, A. Medvids, J.-J. Huang, C.-Y. Chen, C.-H. Liao, and C.C. Yang, "*Spatially-Resolved Study of Defect-Related Luminescence in Laser-Annealed InGaN Epilayers*", Program and Abstract Book of the 41st "Jaszowiec" International School and Conference on the Physics of Semiconductors, June 8-15, 2012, Krynica-Zdroj, Poland, p. 111 (poster presentation).

C11. **D. Dobrovolskas**, G. Tamulaitis, J. Mickevičius, C.W. Huang, C.Y. Chen, C.H. Liao, C. Hsieh, Y.L. Jung, D.M. Yeh, C.C. Yang, „*Plasmon-Enhanced Photoluminescence in InGaN Quantum Wells*", Book of Abstracts of the 14-th International Summer School-Conference Advanced Materials and Technologies, 27-31 August 2012, Palanga, p. 74 (poster presentation, **awarded for the best poster)**.

C12. J. Mickevicius, **D. Dobrovolskas**, G. Tamulaitis, C.-W. Huang, C.-Y. Chen, C.-H. Liao, C. Hsieh, Y.-L. Jung, D.-M. Yeh, and C.C. Yang, "*Spatial distribution of surface-plasmon-enhanced photoluminescence in InGaN/GaN quantum wells"* Final program of the 31st International Conference on the Physics of Semiconductors (ICPS-2012), July 29-August 3, 2012, Zurich, Switzerland, p. 122 (poster presentation).

C13. J. Mickevicius, **D. Dobrovolskas**, R. Aleksiejunas, A. Kadys, T. Malinauskas, T. Grinys, and G. Tamulaitis, "*Carrier localization in graded-shape InGaN/GaN quantum wells*", Program and Exhibition Guide of International Workshop on Nitride Semiconductors (IWN-2012), October 14-19, 2012, Sapporo, Japan, p. 49 (poster presentation).

C14. **D. Dobrovolskas,** A. Vaitkevičius, J. Mickevičius, Ö. Tuna, C. Giesen, M. Heuken, G. Tamulaitis, *„Įtemptų ir relaksavusių InGaN epitaksinių sluoksnių liuminescencijos erdvinis pasiskirstymas"*, 40-oji Lietuvos nacionalinė fizikos konferencija, birželio 10-12 d. 2011 m., Vilnius, Programa ir pranešimų tezės, p. 102 (poster presentation)

C15. A. Vaitkevičius, **D. Dobrovolskas,** J. Mickevičius, Ö. Tuna, C. Giesen, M. Heuken, G. Tamulaitis, *„Kilpinių defektų įtaka InGaN kvantinių lakštų fotoliuminescencijai"*, 40-oji Lietuvos nacionalinė fizikos konferencija, birželio 10-12 d. 2013 m., Vilnius, Programa ir pranešimų tezės, p. 103 (poster presentation)

C16. A. Kalpakovaitė, **D. Dobrovolskas**, M. Dmukauskas, T. Grinys "*Optical Response of Metal Nano-Islands Fabricated on GaN Based Structures*" Book of Abstracts of the 15-th International Summer School-Conference Advanced Materials and Technologies, 27-31 August 2013, Palanga, p. 55 (poster presentation)

C17. R. Tomasiunas, E. Jelmakas, P. Gecys, **D. Dobrovolskas**, A. Kadys, G. Raciukaitis, and S. Margueron, "*GaN epitaxial lateral overgrowth of laser patterned*", Program and Exhibit Guide of 10-th International Confenference on Nitride Semiconductors (ICNS-10), August 25-30, 2013, Washington, DC, USA, p.98 (poster presentation).

C18. S. Nargelas, **D. Dobrovolskas,** J. Mickevicius, M. Vengris, R. Aleksiejunas, G. Tamulaitis, H.-S. Chen, C.-F. Chen, C.-Y. Chen, C.-H. Liao, and C.C. Yang, "*Space- and time-resolved spectroscopic study of InGaN/GaN quantum wells coupled with the localized surface plasmons in metal nanoparticles*" Program and Exhibit Guide of 10-th International Confenference on Nitride Semiconductors (ICNS-10), August 25-30, 2013, Washington, DC, USA, p.165 (poster presentation).

2. Properties of InGaN epilayers and heterostructures

Among the ternary compounds of group III nitrides, InGaN has attracted attention of scientific community due to its potential applications as well as unique material properties. However, some of the fundamental properties of InGaN materials are still not well understood. For example, only recently the band gap of InN has been experimentally shown to be around 0.7 eV, substantially narrower than previously thought (~1.9 eV). Therefore, most of the results on InGaN reported prior to 2002 have to be reevaluated.

In this chapter, the structural and electronic properties of InGaN are briefly reviewed. Features and issues of III-nitrides growth by MOCVD technique are also discussed. It is shown that photoluminescence spectroscopy is a powerful technique to study InGaN properties.

2.1. Structural and electronic properties of InGaN

Group III nitrides can crystallize in one of three crystalline structures: wurtzite, zinc blende, and rock-salt [1]. However, the major interest is in wurtzite nitrides because of their thermodynamically stable phase. The wurtzite structure is shown in Fig. 2.1. In nitrides, each nitrogen atom is coordinated by four group III atoms which are positioned at the peaks of a tetrahedron. The structure has a hexagonal unit cell, which is characterized by two lattice constants, *c* and *a*. The lattice constants are *a*=3.189 Å and *c*=5.186 Å for GaN and *a*=3.538 Å and *c*=5.703 Å for InN [1]. According to Vegard's law, the lattice constants for ternary $In_xGa_{1-x}N$ alloy can be interpolated between those of GaN and InN by assuming a linear change with alloy composition:

$$\begin{aligned} c(In_xGa_{1-x}N) &= (1-x)\cdot c(GaN) + x\cdot c(InN) \\ a(In_xGa_{1-x}N) &= (1-x)\cdot a(GaN) + x\cdot a(InN) \end{aligned} \qquad (2.1)$$

Hence, Vegard's law allows estimating alloy composition from X-ray diffraction (XRD) measurements of its lattice constant (and *vice versa*).

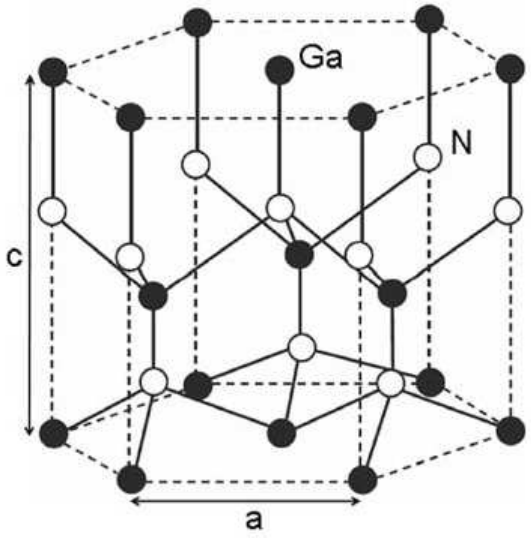

Fig. 2.1. Wurtzite GaN crystal with Ga-face[2].

The wurtzite structure consists of two interpenetrating hexagonal close-packed sublattices, each with one type of atoms, offset along the c-axis by 5/8 of the cell height. The stacking sequence of the (0 0 0 1) planes is ABAB in the <0 0 0 1> direction.

The wurtzite nitrides lack an inversion plane perpendicular to the c-axis; thus nitride surface have either a group III element (Al, Ga, or In) polarity (referred as Ga-face) or a N-polarity (N-face). As a result, nitrides exhibit highly pronounced polarization effects.

All group III nitride semiconductors have a direct band gap. At $k = 0$, the valence band is split by the combined effect of crystal field and spin-orbit coupling into three bands designed as A, B, and C bands. For GaN, the energy difference between A and B bands (spin-orbit splitting) is $\Delta E_{AB} = 8$ meV and the difference between A and C bands (crystal-field splitting) is $\Delta E_{AC} = 40$ meV. In InN the spin-orbit splitting and crystal-field splitting are estimated to be $\Delta E_{AB} = 5$ meV and $\Delta E_{AC} = 40$ meV, respectively [3].

The band gap of group III-nitride as a function of lattice constant is shown in Fig. 2.2. The band gap of InN was long thought to be 1.9 eV. Only recently, when higher crystal quality of InN was achieved, the band gap was reevaluated to ~0.7 eV [4]. This discrepancy was explained by Burstein-Moss shift. Early InN samples typically contained high carrier concentration due to high density of donor impurities. It caused Fermi level to rise up into the conduction band. Consequently, the absorption edge is pushed to higher energies since all the states below Fermi level are occupied. Thus optical absorption measurements of InN indicated erroneous band gap values.

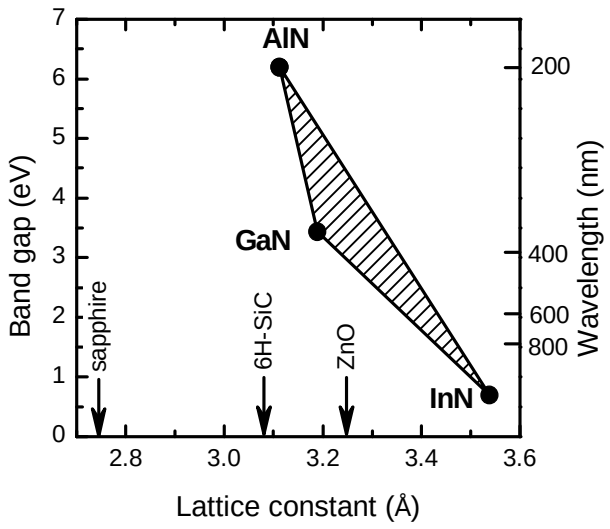

Fig. 2.2. The band gap of the group III-nitrides alloys as a function of lattice constant. Lattice constants of substrates are indicated by arrows.

The band gap of ternary InGaN alloy is a function of In content and can be expressed using the following expression:

$$E_g(In_xGa_{1-x}N) = x \cdot E_g(InN) + (1-x) \cdot E_g(GaN) - b \cdot x(1-x), \quad (2.2)$$

where b is a bowing parameter. The bowing parameter accounts for the deviation from a linear interpolation between the two binaries GaN and InN. Earlier reports must be reevaluated, after the band gap of InN was corrected. Recent theoretical calculations suggest b=1.51 [5], which is consistent with experimental results ranging between b=1.43 [6] and b=1.65 [7]. Moreover, an interesting universal behavior of the bowing parameters of group III nitride alloys has been observed. The ratio of the bowing parameter and the band gap difference of the binaries ($b/|E_g(InN)-E_g(GaN)|$) approximately equals 0.5 [8]. For InN, it results in the bowing parameter value b=1.35 and is in good agreement with the reported values [5–7].

2.2. MOCVD growth of III-nitrides

One of the most common growth techniques, used both for a scientific and commercial purpose, is metalorganic chemical vapor deposition (MOCVD), also known as metalorganic vapor phase epitaxy (MOVPE). A simplified view of MOCVD system is shown in Fig.2.3.

MOCVD is non-equilibrium growth technique, which relies on vapor transport of the precursors and subsequent reactions at elevated temperatures in the reactor resulting in the deposition of materials on the substrate. Trimetilgallium (TMGa), triethylgallium (TEGa), trimethylaluminum (TMAl), trimethylindium (TMIn), and other metalorganic compounds are used as III

metal precursors. Regarding the group V precursor, ammonia (NH_3) is usually used for III-nitride growth. Silane and bis-cyclopentadienyl-magnesium (Cp_2Mg) are commonly used for *n* and *p*-type doping, respectively.

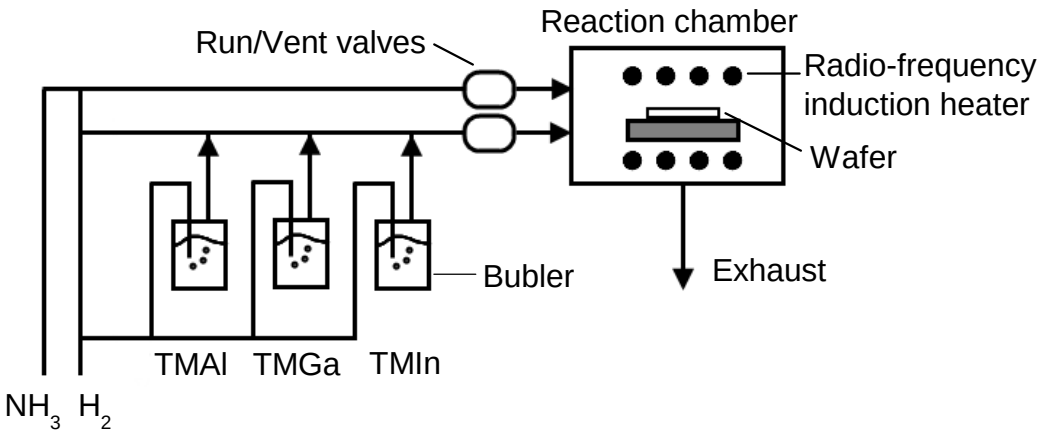

Fig. 2.3. A scheme of a metalorganic chemical vapor deposition (MOCVD) system.

The metalorganic sources are stored in devices, called bubblers, through which a carrier gas (typically hydrogen or nitrogen) flows. The amount of metalorganic vapor transported depends on the rate of carrier gas flow and the bubbler temperature. The carrier gas saturates with vapor from the source and transports the vapor to the heated substrate in the reaction chamber. For InN growth, temperatures above 550˚C are required. Even higher temperatures up to, or above 1000˚C are required for GaN growth. To achieve such high temperatures, a substrate holder is equipped with radio frequency heater or resistance heater. At the same time, the chamber walls are kept colder to minimize wall deposits and reduce reactant depletion.

2.3. Growth issues

The growth of nitride materials exhibit particular issues that deteriorate crystal quality and, hence, decrease device efficiency. First of all, there is a lack of low-cost native substrates for III-nitride growth. The best available alternative substrates are ZnO and SiC, however, most epitaxial growth of III-nitride materials is performed on sapphire substrate. This material is a substrate of

choice due to its high quality and availability in large quantities. In addition, it is transparent to UV and visible light. The (0 0 0 1), or basal plane, is the most commonly used surface for III-nitride growth. Crystal orientations of sapphire and GaN (grown on *c*-plane [0001] sapphire) are parallel but the unit cell of GaN is rotated by 30˚ around the *c* axis with respect to the sapphire unit cell. The main disadvantage of the substrate is a large (~15%) lattice mismatch between GaN and sapphire [9]. As a result, the crystalline quality of epilayers grown directly on sapphire is quite poor, the layers contained high density of dislocations. One of the major breakthroughs in the epitaxial growth was achieved by the introduction of a low-temperature GaN or AlN buffer layer before the formation of the following structure. The buffer layer can greatly reduce the dislocation density by limiting the dislocation penetration into the structure.

Another difficulty of growing InGaN alloys arises from contrasting thermodynamic properties of InN and GaN. Due to low dissociation temperature and high volatility of InN, InGaN growth needs to be performed at lower temperatures than that of GaN growth. InGaN QWs are typically grown at 700 – 800 ˚C or even at lower temperatures to ensure incorporation of high content of indium into the structure. The temperature is much lower than the optimal growth temperature of GaN. As a result, during the subsequent growth of *p*-type layers, the InGaN quantum wells may suffer from indium re-evaporation and inter-diffusion [10].

The growth of high quality InGaN structures is also complicated by a solid phase miscibility gap that usually results in phase separation in InGaN epilayers and structures with high indium content. Early theoretical calculations showed that the solubility of InN in GaN is only about 6% and the miscibility gap covers almost entire composition range [11]. However, as revealed later, the phase separation may be considerably suppressed by the lattice strain produced during the epitaxial growth [12]. This can explain the repeated growth of InGaN samples with In content up to 30% without phase separation [13,14]. However, the growth of InGaN structures containing higher

In percentage remains challenging. Despite these issues, single phase InGaN layers containing In composition ranging from 25% to 63% were recently grown using MOCVD technique [15]. The high quality of the high In content InGaN layers was confirmed by XRD measurements. The presence of lattice strain, the nonequilibrium nature of MOCVD growth process, and low growth temperatures ($730 - 610^{\circ}C$) are attributed to the main factors ensuring the suppression of the phase separation. This suggests that it is possible to synthesize single phase InGaN alloys inside the compositions range that was previously thought to be within the miscibility gap.

III-nitrides exhibit highly pronounced polarization effects. The lack of center symmetry in group-III nitrides results in piezoelectricity. The piezoelectricity effect has two components. One is due to lattice mismatch strain, while the other is due to thermal strain caused by different thermal expansion coefficient of the substrate and the epitaxial layers. Nitrides also exhibit spontaneous polarization with polarity determined by which plane, anion or cation, is on the surface. In bulk crystals, charges occurring due to spontaneous polarization compensate each other. However, at the interface between two nitride semiconductors with different polarization, the charges are uncompensated. This, in addition to the strain induced piezoelectricity, creates internal electric field [9].

The piezoelectric polarization field is strain depended. It increases with lattice mismatch between the quantum well and the barrier or substrate material. Therefore, it becomes more pronounced as the indium content is increased in InGaN/GaN quantum wells. However, internal electric field is not desirable for LEDs. As the internal electric field is increased, the band structure of a quantum well is tilted and the quantum well is transformed from rectangular to triangular shape. This results in the narrowing of effective bandgap and spatial separation of electron and hole wave functions. The effect is called quantum-confined Stark effect (QCSE). Due to separation of carrier wave functions, the transition probability for recombination is significantly decreased. The QCSE leads to an increase in the radiative carrier lifetime and,

consequently, decreases the efficiency of the luminescence in the active region [16–18].

2.4. Spatial inhomogeneity of photoluminescence properties

It is generally accepted that the carrier localization arising from spatially inhomogeneous indium distribution plays an important role in spontaneous emission from InGaN. The compositional fluctuations occur as a result of large contrasts in the thermodynamic and structural properties of GaN and InN, leading to a large miscibility gap, as mentioned in section 2.3. The compositional fluctuations in InGaN alloy results in bandgap fluctuations that localize carriers. Since the potential fluctuations occur at the same spatial position for both electron and hole, the localized carriers are often referred to as excitons. Therefore, the exciton localization by band potential fluctuation prevents carriers from reaching nonradiative recombination sites. This explains, why, despite poor material quality of the alloy, the InGaN-based LEDs are relatively efficient.

In addition to inhomogeneous distribution of indium content, potential fluctuations in InGaN MQWs can also originate due to well width variation [19] and inhomogeneity of piezoelectric polarization field [20]. All these effects can localize excitons and contribute to spatial inhomogeneity of PL properties.

The carrier localization manifest itself by a characteristic S-shaped PL band peak position shift as the temperature is changed [21,22]. At low temperatures ($T<60$ K), the PL band initially redshifts due to the thermally enhanced hopping of excitons into the lowest available energy sites. As the temperature increases, excitons gain enough kinetic energy to populate higher localized states. This results in a blueshift of the PL band. Finally, at sufficiently high temperatures, the PL peak shifts to longer wavelengths, because the temperature-induced bandgap shrinkage starts to dominate.

The average potential fluctuations due to inhomogeneous distribution of indium content can be evaluated from the temperature dependences of PL spectra. Moreover, after the comparison of the experimental results and Monte Carlo simulation of exciton hopping, it was suggested, that InGaN alloy exhibits a double-scaled potential fluctuation: small-scale fluctuations exist within large-scale fluctuations of In-rich areas [21,22].

To better understand the exciton localization in InGaN, the spatially resolved luminescence is investigated by cathodoluminescence (CL) mapping, confocal microscopy, and scanning near field optical microscopy (SNOM). However, the spatial scale of potential fluctuations is still not clear. For instance, CL mapping images of InGaN show areas of high luminescence intensity (bright spots) that range from 60 nm to 400 nm in diameter [23–25]. Moreover, the dimension of lateral CL intensity variations increased in samples of higher indium content [25]. This implies a compositional undulation at sub-micrometer scale. Indeed, a structural change in InGaN MQWs was directly observed using transmission electron microscopy (TEM). Numerous papers reported that InGaN quantum wells contain dots of 2 nm to 5 nm in diameter [26–28]. These areas were attributed to self-formed indium rich clusters. However, a more comprehensive TEM study later revealed that InGaN quantum wells are very sensitive to electron beam damage. Thus, a short electron beam exposure creates inhomogeneous lattice strain that had been falsely attributed to indium clustering [29]. Even CL microscopy, which uses much lower electron beam energy than that in TEM, induces a long lasting change in spatial distribution of luminescence [30].

Alternatively, confocal optical microscopy can be employed to analyze the spatial distribution of luminescence. However, the spatial resolution of confocal microscopy is lower than that of CL microscopy. Nevertheless, confocal microscopy also shows inhomogeneous PL distribution in InGaN [31–34]. A typical diameter of bright spots ranges from 200 nm to 1 µm. PL band peak in the bright spots should be at longer wavelengths compared to its position in areas of lower PL intensity, as it is expected from

carrier localization by indium content fluctuations. Meanwhile, a strong positive correlation between PL intensity and peak wavelength is observed in InGaN samples with relatively low indium content (x<15%) [35]. No clear correlation can be specified as the indium content is increased [32]. Moreover, the correlation becomes negative as the indium content is further increased. In InGaN MWQs with high indium content (x>30%), the areas of high PL intensity have shorter wavelengths, while the areas of low PL intensity emit at longer wavelengths. This indicates contribution of additional effects influencing inhomogeneous distribution of PL intensity. It was suggested, that the size of indium-rich areas depends on the average indium content and these areas are larger in samples of high indium content. Thus, the localization of excitons in the indium-rich areas is weaker. Moreover, QCSE is more pronounced as the indium content is increased in InGaN quantum wells. Therefore, the delocalization of carriers and the reduction of electron and hole wave functions overlap due to QCSE are pointed out as the main mechanism of the reduced PL intensity at long wavelengths [35].

Scanning near-field optical microscopy (SNOM) provides even higher spatial resolution than it can be achieved with CL or confocal microscopy. The spatial PL intensity distribution in InGaN layers and MQWs is found to have a similar pattern as it was previously observed by CL or confocal microscopy. A typical reported diameter of bright spots varies from 100 nm to 1 μm [36–38]. Again, SNOM measurements revealed that PL intensity and band peak wavelength correlation is indium-content-dependent. For InGaN MQWs of small In composition (x<8%) [39,38], the correlation is positive, but it turns negative in InGaN MQWs of high In content (x>25%) [40]. It was concluded that the different correlations are caused by indium-content induced potential fluctuations that influence the probability for carriers to reach nonradiative recombination centers, such as threading dislocations.

A simultaneous measurement of PL intensity and sample roughness is another advantage of SNOM. By comparing a topographic image and PL intensity distribution, the areas of low PL intensity coincide well with V-

shaped defects which are associated with mixed or screw dislocations [41,42]. Further investigations revealed high band edge PL intensity around the perimeter of the V-defect and weak impurity related luminescence inside the defect [42,43]. TEM images showed that dislocations and impurities gather in the vicinity of the V-defect. Impurity complexes are known to have energies deep within the band gap and are the source of yellow emission in GaN [44]. This explains why impurity related luminescence is observed inside the V-defects. On the other hand, it was also suggested that the V-defect is surrounded by regions of higher band gap, which inhibits nonradiative carrier recombination inside the defect [45]. The higher potential region arises due to the formation of the narrower quantum wells on the facets of the V-defect.

In summary, in spite of the progress currently achieved in characterization and growth of GaN, the development of InGaN-based devices is still difficult. Growth issues, particularly for high indium content InGaN heterostructures and epilayers, are in a need of a breakthrough. It is evident that compositional and structural undulations contribute to spatial inhomogeneity of photoluminescence properties. A better understanding of contribution of these properties is required for further improvement of the efficiency of InGaN-based devices. A considerable progress can be achieved by studying luminescence at the sub-micrometer scale by SNOM or confocal microscopy, which gives a direct insight into radiative and nonradiative carrier recombination processes in III-nitrides.

3. Experimental setup

3.1. Techniques for spatially-resolved PL study

Scanning confocal microscopy has become an invaluable tool for a wide range of investigations due to its relatively simple and inexpensive technique for achieving a high spatial resolution. Confocal microscopy offers several advantages over conventional optical microscopy, including shallow depth of field, elimination of out-of-focus emission, and the ability to collect several optical sections from thick specimens [46,47].

In a conventional wide field microscope, the entire area of interest of the sample under study is illuminated from a light source, and the image can be viewed directly by eye or projected onto an image capture device. In contrast, the method of image formation in a confocal microscope is fundamentally different. The goal in confocal microscopy illumination is to focus the excitation light into a spot as small as possible. The luminescence is collected from that single excited spot. Thus, to create the image, the area of interest is examined point by point either by moving the excitation beam or the sample.

The typical configuration of the confocal microscope is shown in Fig. 3.1. The excitation beam is focused and the luminescence is collected using the same objective. The luminescence is reflected by a beam splitter and is focused into the detector. However, before the signal is detected, it has to pass a small aperture (pinhole) which is in front of the detector. The pinhole spatially filters out the light originating from the parts of the sample which are not in the focal plane of the objective. As a result, both the resolution and the image contrast are improved.

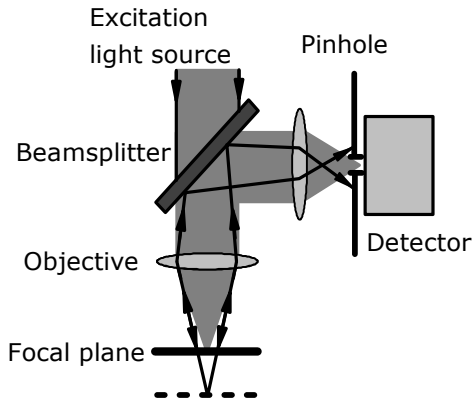

Fig. 3.1. The configuration of confocal microscope.

The spatial resolution of optical microscopes depends on the wavelength λ of the light

used and the numerical aperture (NA) of the objective. For the confocal microscope, the lateral resolution d_{xy} can be approximated as

$$d_{xy} = 0{,}4\frac{\lambda}{NA}, \tag{1}$$

where the numerical aperture $NA = n \cdot \sin\theta$, n is a refraction index of the medium between the sample and the objective, and θ is the half angle of the light cone that enters the objective. The lateral resolution of confocal microscope is improved by a factor of ~1.5 in comparison to that of conventional microscope [48].

As only the light coming from the focal plane is detected, the axial resolution in confocal microscopy is also improved and optical sectioning of the sample can be achieved. By scanning at different focal planes, a three dimensional image of the sample can be created. The spatial resolution along the z-axis can be approximated as

$$d_z = 1{,}4\frac{\lambda}{NA^2}. \tag{2}$$

However, the resolution of optical microscopes is diffraction-limited to about a half wavelength. This limit can be exceeded using scanning near-field optical microscopy (SNOM) by exploiting properties of the evanescence waves which exist only near the surface of the photoexcited object [49]. Because the field decreases with the distance r as $1/r^6$, the probe containing a small aperture is placed close to the surface of the sample (Fig. 3.2). Both the diameter of the aperture and the distance to the sample is smaller than the

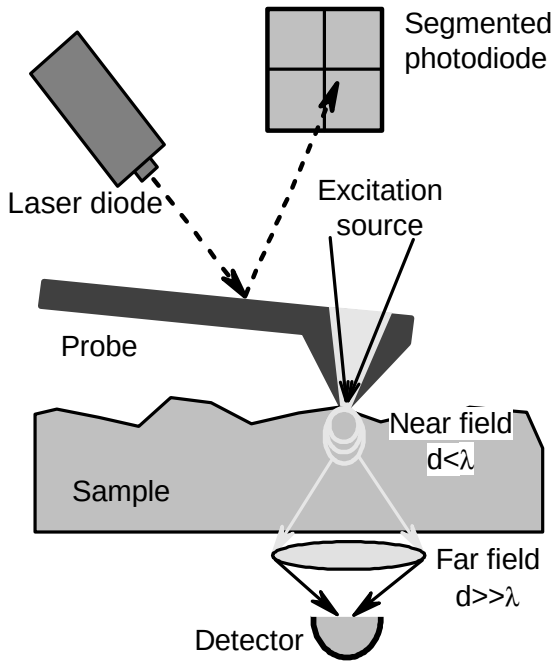

Fig. 3.2. The configuration of scanning near-field optical microscope (SNOM).

wavelength. The image is created by raster scanning the probe over the sample surface. In contact mode, the distance between SNOM probe and the sample is controlled by a feedback system similar to that used in atomic force microscopy (AFM): a second laser is focused onto the probe and the reflected signal is detected with a segmented photodiode. The position of the laser beam on the photodiode changes as the probe bends during the surface scan. The feedback electronics holds the probe bending fixed during the scan using a digital closed loop controller. The change in position is registered and used to correct the distance between the probe and the sample. Thus, the SNOM technique can analyze optical and surface topography of the sample simultaneously.

The optical resolution of SNOM is determined by the diameter of the aperture. Thus resolution smaller than the diffraction limit can be achieved. However, the light transmission through the aperture rapidly decreases with aperture size. Therefore, a trade-off between signal the strength and resolution has to be considered. Usually the aperture of ~100 nm is used in SNOM measurements.

There are several SNOM set-up configurations. In illumination mode, the sample is excited through the probe and the luminescence is detected in the far field (Fig. 3.2). The collection mode uses far field excitation while the luminescence is collected by the probe in the near field. In illumination-collection mode, excitation and collection are accomplished through the probe.

Although surface topography can me analyzed by SNOM, the spatial resolution is usually worse than that of AFM. The AFM probes do not have an aperture, thus the tip of the probe can be made extremely sharp. As a result, AFM can resolve smaller details, and measurements with resolution of single atoms can be performed. On the other hand, sharp AFM tips (~1 nm) tend to wear fast during measurements. Therefore, relatively larger AFM probe tips of ~10 nm are more robust.

3.2. Experimental setup

Spatially-resolved PL study was performed using *WITec* microscopy system *Alpha 300* enabling measurements in three different modes: confocal, SNOM and AFM. A He-Cd laser (λ_{exc}=442 nm) or a laser diode (λ_{exc}=405 nm) were used as excitation sources. The laser beam is focused into a spot of ~300 nm in diameter. PL spectra were recorded using the spectrometer *UHTS 300* equipped with a thermo-electrically cooled CCD camera. All the spatially-resolved PL measurements were made at room temperature.

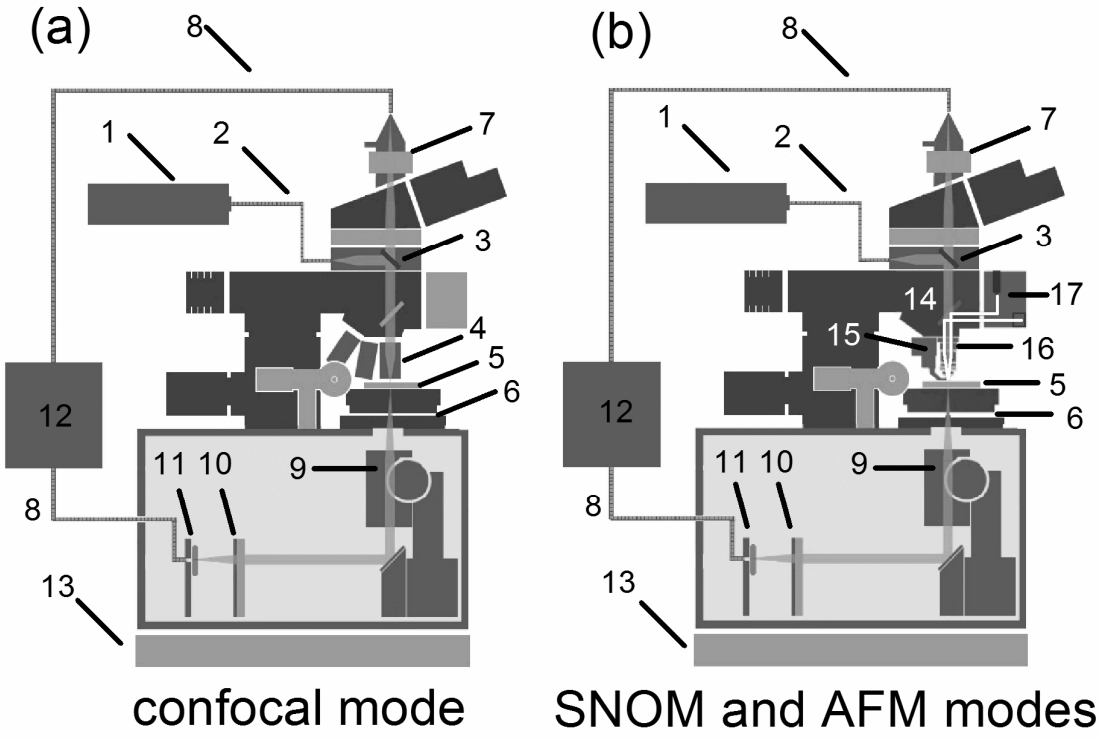

Fig. 3.3. Experimental setup for spatially-resolved PL measurements in confocal mode is shown in (a): 1 – laser; 2 – single-mode fiber; 3 – beam splitter; 4 – objective; 5 – sample; 6 – scan table; 7 and 11 – long-pass filter; 8 – multi-mode fiber; 9 – objective; 10 – focusing lens; 12 – spectrometer with CCD camera; 13 – active vibration isolation system. Experimental setup for SNOM and AFM measurement modes is shown in (b): 14 – dichroic mirror 15 – SNOM or AFM probe; 16 – objective; 17 – beam deflection unit.

Figure 3.3(a) shows the beam path in PL measurements in confocal mode. The laser (1) beam is coupled into the optical fiber (2), which is connected to the microscope. A collimated laser beam is focused onto the sample by an

objective (4) of high numerical aperture. The sample (5) is placed on the piezoelectric scaning stage (6). It has a minimum step size of 1 nm and the maximum scan range of 80 µm. The PL signal from the sample is collected by the same objective (4) and passes a long-pass filter (7). At the top of the microscope, the signal is focused into a multi-mode optical fiber (8). The core of this fiber acts as a pinhole for confocal microscopy. The fiber directs the signal into the entrance slit of the spectrometer coupled with a CCD camera (12). Alternatively, the PL signal can be collected in transmission mode by objective (9) and is focused by a lens (10) into the multi-mode optical fiber (8). The PL spectra are recorded by the spectrometer coupled with a CCD camera (12). For isolation against low frequency vibrations, the entire microscope is mounted on an active vibration isolation system (13). All the measurements and data accusations are computer controlled through the *WITec Control* software.

The scheme of SNOM and AFM measurements module is shown in the Fig. 3.3(b). The objective (16) is used to focus the excitation laser beam as well as a feedback laser beam onto the probe (15). The PL signal is collected in transmission mode, as described above. Control of the distance between the probe and sample in SNOM and AFM modes is accomplished using a beam deflection unit (17) consisting of a feedback laser diode (λ = 980 nm) and a segmented photodiode. AFM or SNOM probes are fabricated on a 700 µm long and 150 µm wide cantilever that is magnetically fixed on a larger mount. The SNOM probe is pyramid shaped with a base of 20 µm and height of 15 µm. At the center of the pyramid, the probe has a nanoscopic hole of 100 nm in diameter, which acts as the near field aperture. The AFM probe has a sharp tip of ~10 nm. Both SNOM and AFM measurements are performed in contact mode.

4. Critical thickness for strain relaxation in InGaN epilayers and influence of strain on PL properties

4.1 Topic review

Native substrates are not available for InGaN. Therefore, structural quality of the InGaN heteroepitaxial layers is still the key issue in the production of InGaN-based devices. GaN buffer layers are often used when growing the InGaN on sapphire substrate. However, the lattice constant of InN is larger than that of GaN. Therefore, this heteroepitaxial growth results in a large strain in the InGaN epilayer grown on GaN. Beyond a certain critical layer thickness, when no more strain can be accommodated by the lattice, InGaN layer relaxes by generating defects and, consequently, decreasing the crystal structural quality [9].

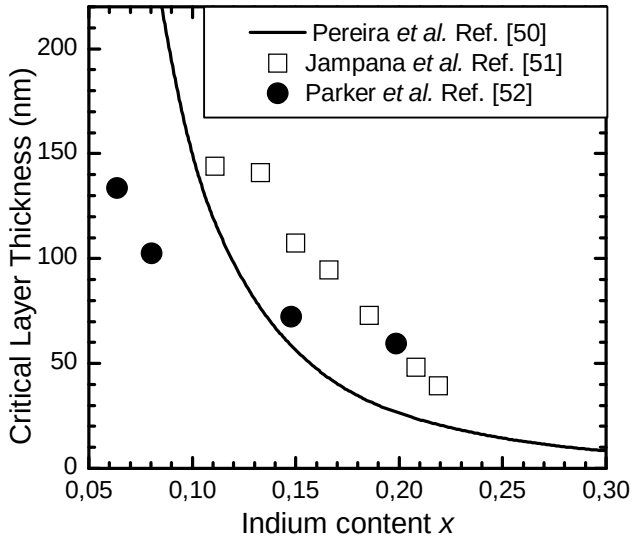

Fig. 4.1. The comparison between theoretical critical layer thickness values (solid line) [50] with those obtained experimentally (symbols) [51,52].

The critical layer thickness of InGaN can be estimated using a theoretical model proposed by People and Bean, as described in Ref. [50]. Figure 4.1 shows that the critical layer thickness rapidly decreases with increasing indium content because of the increasing lattice mismatch. A large discrepancy between calculated and experimental values is usually attributed to the lack of the knowledge of InGaN elastic properties and the approximation involved in the theoretical models.

There are several experimental techniques to determine the critical thickness. The layer relaxation alters crystal lattice constant which can be directly evaluated using X-ray diffraction (XRD) technique. Numerous publications report that InGaN layers do not relax uniformly. Broad and even

double XRD peaks are often observed and interpreted as originating from two InGaN sub-layers: a strained layer adjacent to GaN/InGaN interface, and partially or fully relaxed one on the top of it [53–57]. Spatially resolved cathodoluminescence and energy dispersed X-ray (EDX) measurements show that the strained layer contains less indium than the relaxed one [54,56,57]. It is assumed, that during the early stage of the InGaN layer growth on lattice-mismatched substrate indium atoms tend to be excluded from the InGaN layer to reduce the lattice strain. This effect is known as compositional pulling. However, sometimes the compositional variation along the layer growth direction was not observed and the double XRD peaks were attributed only to strain variation [55].

In addition to XRD, photoluminescence spectroscopy technique can also be used to determine the critical layer thickness. The band gap of strained layers is expected to be larger than that of relaxed layers due to compressive lattice stresses [50,58]. Therefore, as the layer thickness increases, the redshift of the PL peak indicates the onset of the layer relaxation.

In this chapter, the study of in-plane inhomogeneities of InGaN layer properties imposed by strain and its relaxation is presented. Extensive analysis is made by comparing results on layer structure obtained by XRD, study of layer surface by atomic force microscope (AFM), and mapping of photoluminescence (PL) parameters by using spatially-resolved spectroscopy via confocal microscope.

4.2 Samples and measurement techniques

The InGaN epilayers under investigation were grown on sapphire substrate with a 5 µm GaN buffer layer by MOCVD technique at AIXTRON SE using an AIXTRON 3x2” Close-Coupled Showerhead reactor. Two sets of samples were fabricated for the study. Set A of four 50 nm-thick epilayers was grown at different deposition temperatures to obtain $In_xGa_{1-x}N$ samples with different indium content: 17, 19, 21, and 23% for samples A17, A19, A21, and A23,

respectively. In sample set A, epilayer thickness was below the critical value in the samples with lower In content and above the critical value for the samples with higher In content. The sample set B consisted of three $In_xGa_{1-x}N$ layers with approximately the same indium content (x~17%) but different layer thickness: 90±5, 135±8, and 150±10 nm in samples B90, B135, and B150, respectively. All layer thicknesses in sample set B are above the critical value. The strain states of the layers were studied by means of X-ray diffraction (XRD) reciprocal space mapping (RSM) of (10-15) diffraction. The In contents of the layers were determined by comparison of XRD measurements with simulations.

The spatial distribution of PL intensity in InGaN layers was studied on a submicrometer scale using *WITec* microscope system *Alpha* 300 operated in confocal mode. For spectral resolution, the microscope was coupled by an optical fiber with a *UHTS300* spectrometer followed by a thermoelectrically cooled CCD camera. The excitation beam of a CW laser diode emitting at 405 nm was focused onto the sample using high numerical aperture (NA = 0.9) objective. This ensured in-plane spatial resolution of approximately 250 nm. PL excitation power density was kept constant at 230 kW/cm^2. The sample surface topography has been investigated by the same microscope system *Alpha* 300 operated in atomic force microscope mode with spatial resolution of ~10 nm. The thicknesses of the InGaN layers were estimated by scanning electron microscopy (SEM).

4.3 Influence of strain and its relaxation on PL properties in InGaN epilayers below and above the critical thickness

The layer relaxation in the samples under study was observed by XRD reciprocal space mapping (RSM) of (10-15) diffraction accomplished at AIXTRON SE. Figure 4.2 shows RSMs of 50 nm thick $In_{0.17}Ga_{0.83}N$ layer (sample A17) and 150 nm $In_{0.17}Ga_{0.83}N$ layer (sample B150). The diffraction spot of InGaN layer is observed below the strong peak of GaN buffer layer. Up

to the critical layer thickness, the in-plane lattice of InGaN layer matches that of the underlying GaN buffer layer. In Fig. 4.2(a), the center of InGaN diffraction spot of sample A17 (as well as that of samples A19 and A21, not shown) coincides with that of GaN buffer (difference in reciprocal lattice unit $\Delta Q_x = 0$) [51,59]. The small radius and circular shape of the InGaN diffraction spot indicate that these InGaN layers are structurally homogeneous [57]. Beyond the critical layer thickness, the strain cannot be accommodated by the lattice, and the InGaN layer becomes relaxed. This case is demonstrated by RSM of 150 nm thick $In_{0.18}Ga_{0.82}N$ layer (sample B150) in Fig. 1(b). Note that the center position of the InGaN diffraction spot does not coincide with that of GaN ($\Delta Q_x \neq 0$). This shows that the in-plane lattice of the InGaN layer is no longer coherent to GaN, as a result of layer relaxation. The significantly broader diffraction spot of InGaN layer in Fig. 4.2(b) might be attributed to the defects created in the relaxed layer and to the variations of indium content or strain.

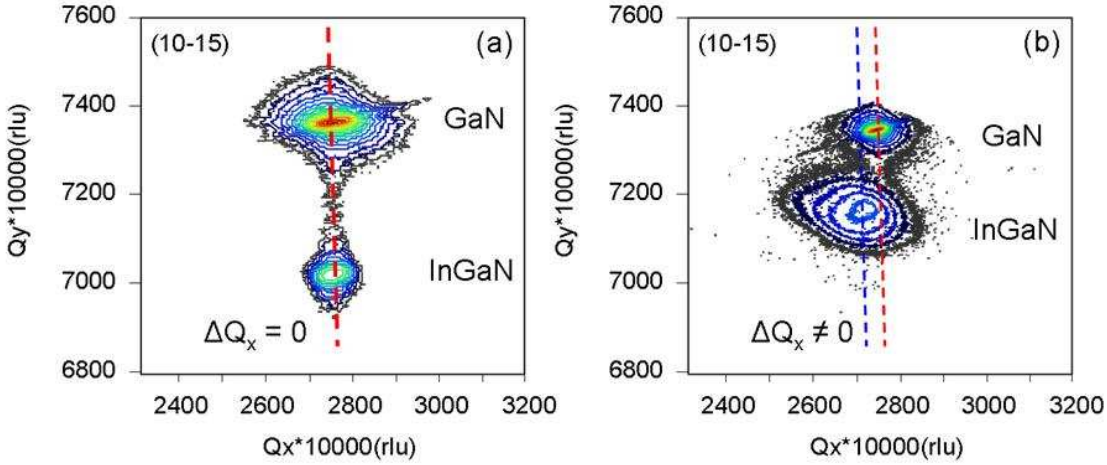

Fig. 4.2. Reciprocal space maps of 50 nm-thick $In_{0.17}Ga_{0.83}N$ layer (sample A17) (a) and 150 nm-thick $In_{0.17}Ga_{0.83}N$ layer (sample B150) (b). [P2]

The changes in the layer structure can also be revealed using PL spectroscopy measurements. Spatially-averaged PL spectra from $10\times10\ \mu m^2$ areas of set A and set B samples are shown in Fig. 4.3. The PL spectra of samples in set A consist of a single band, and the PL band peak position redshifts as indium content increases. Meanwhile, the PL spectra of thick

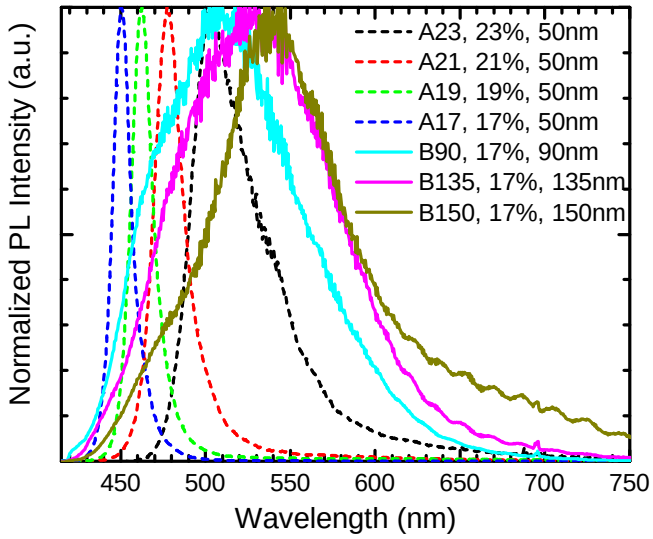

Fig. 4.3. Normalized spatially-averaged PL spectra of series A samples and series B samples. [P2]

layers (sample set B) consist of two overlapping bands: a short-wavelength band peaked close to the peak position of a thin layer with the same In content and a long-wavelength band that has a considerably larger width. These PL features can be understood by taking into account that the compressive lattice stress in strained layers results in a wider band gap and, consequently, in a blue-shifted PL band, as compared with unstrained layer [52]. Thus, we observe the broad long-wavelength band due to emission from the top relaxed layer and a weaker emission component from the strained layer located closer to the buffer. The latter emission is strongly reabsorbed and, consequently, its band is redshifted compared to that of a thin layer.

The critical thickness for lattice relaxation depends on In content [50,55,52]. This trend is observed in set A. PL peak positions and bandwidths of the samples with lower In content (17% to 21% in samples A17 to A21) indicate that these layers are strained (in consistence with the RSM results discussed above). The increase of In content up to 23% results in a further redshift and a considerable broadening of the band. The full width at half maximum (FWHM) of the PL band increases from 13 nm and 20 nm in samples A17 and A21, respectively, to 45 nm in sample A23. The shift and broadening can be explained by increasing In content and lattice relaxation.

The qualitative changes in the layer structure as the layer thickness exceeds the critical value have also been revealed by mapping the spatial distributions of luminescence intensity and peak wavelength. Typical spectrally-integrated PL intensity mapping images of samples A17, A21, and A23 are shown in Fig. 4.4. As it is usual for InGaN epilayers, the spatial distribution of the PL

intensity is strongly inhomogeneous. However, the pattern of the PL distribution depends on In content. Elongated areas of high PL intensity are observed in A17 sample. As the In content is in the range between 19% and 21%, intersecting parallel lines of lower PL intensity are observed [see Fig. 4.4(c)]. This is in consistence with earlier observations that the layer relaxation might be accompanied by the generation of the arrays of misfit dislocations along certain crystallographic planes [60,61]. These dislocations act as nonradiative recombination centers and result in the parallel lines of lower PL intensity observed in a two-dimensional image [see Fig. 4.4(c)]. Further increase in indium content results in formation of bright spots of ~250 nm in diameter on the background with a lower emission intensity.

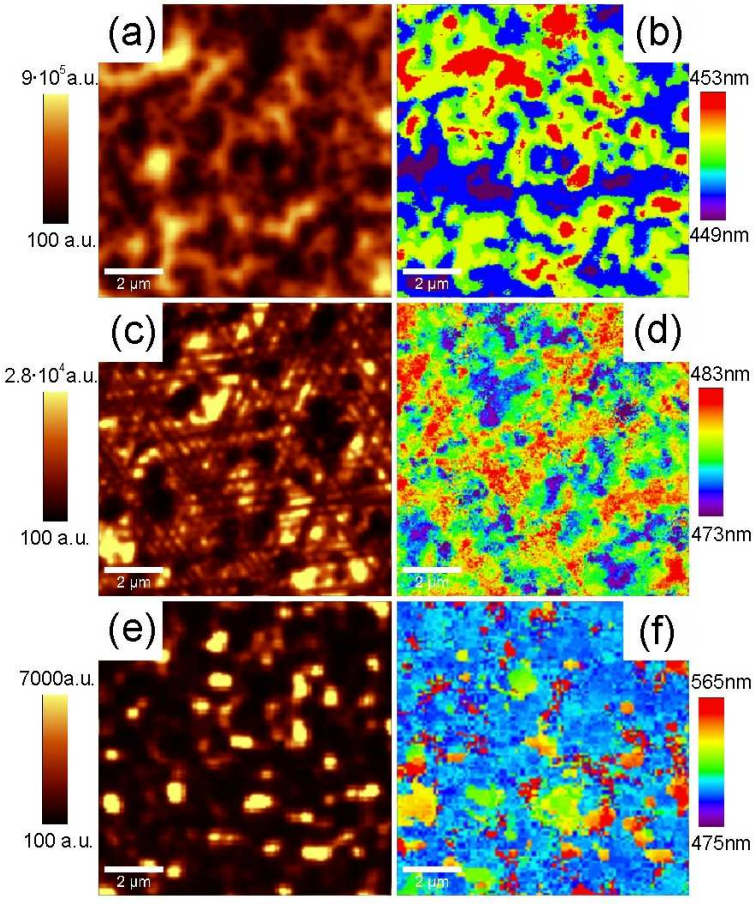

Fig. 4.4. PL intensity and PL peak wavelength mapping images in 10×10 μm^2 area of $In_{0.17}Ga_{0.83}N$ sample A17 [(a) and (b)], $In_{0.21}Ga_{0.79}N$ sample A21 [(c) and (d)], and $In_{0.23}Ga_{0.77}N$ sample A23 [(e) and (f)]. [P2]

Similar features, though not so distinct, can be traced also in the images of peak wavelength mapping [Figs. 4.4(b), 4.4(d), and 4.4(f)]. To evaluate PL

intensity-wavelength relationship, Pearson's correlation coefficient was calculated. The coefficient reflects linear dependence between two variables and may vary between −1 and 1. In sample set A, the Pearson's correlation coefficient is positive ($r = 0.23$) only in sample A17 with low In content (17%), while the coefficient in samples with higher In content is close to zero (indicating no correlation). The correlation of PL intensity and band peak wavelength (positive r) is often observed and usually interpreted by accumulation of carriers in areas with a higher In content [62,36]. The absence of the correlation observed in the samples under study might be caused by contributions of an opposite sign from the lower, strongly stressed sub-layer and a partly relaxed layer on top of it. Meanwhile, the Pearson's correlation coefficient in the thickest, strongly relaxed layers of set B is negative ($r = –0.23$ in B150). The anticorrelation (negative r) might be caused by the higher density of nonradiative recombination centers in the relaxed layer. Inhomogeneous defect distribution has been suggested as the origin of the anticorrelation between PL intensity and peak position in InGaN multiple quantum wells and is discussed in more detail in chapter 6.

To compare PL spectra from different sample areas, we sorted the pixels in the mapped area into several groups exhibiting different PL intensity. The corresponding spectra are presented in Fig. 4.5 for several samples with different In content (A17, A19, A23) and thickness (B135). The vertical dashed lines indicate peak positions of PL band in the corresponding strained layers. In thin layers with low In content (A17, A19 in Fig. 4.5), the peak of the main band corresponds to this position and shows no significant shift in areas of different PL intensity. The weak broad long-wavelength band is clearly distinguishable at the wavelengths higher than 520 nm in figure 4.5(a) and 4.5(b) and might be attributed to defect-related carrier recombination [P5], while band-to-band emission in relaxed areas might also have certain contribution to this band. As discussed above, increase of In content decreases the critical thickness for strain relaxation, and the lattice in the upper part of the layer is relaxed. This results in a new PL band emerging from the relaxed

volume. Position of this line is indicated in Fig. 4.5(c) and 4.5(d) by dotted vertical lines. In sample A23, separation between the two peaks (30 nm) is smaller than that expected due to full strain relaxation. The strain-induced blueshift of the band gap ΔE can be estimated using its dependence on In content x as $\Delta E = kx$ (eV). Values 0.180 eV (39 nm), 0.235 eV (52 nm), and 0.345 eV (81 nm) are obtained for k values 0.79, 1.02, and 1.5 reported respectively in Refs [7,63,64]. Thus, the observed separation can be explained by partial relaxation of the uppermost layer.

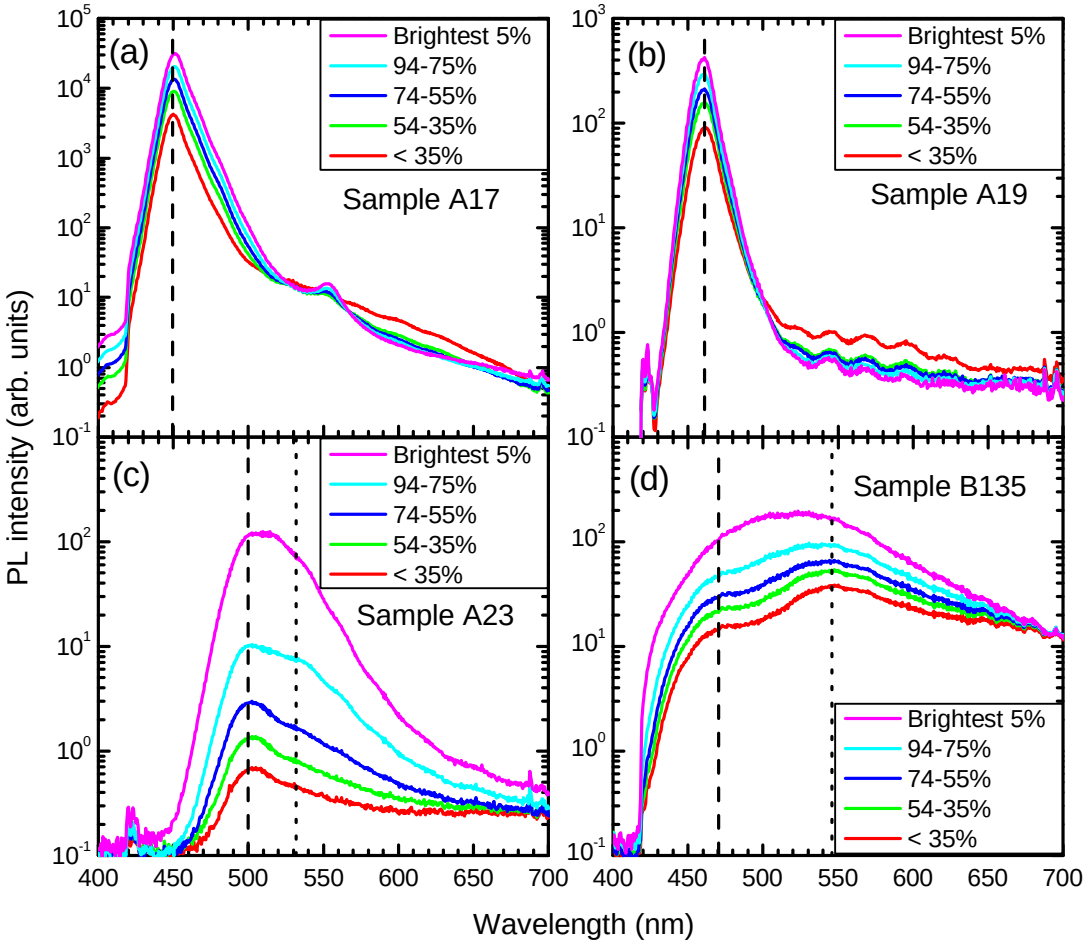

Fig. 4.5. Spatially-averaged PL spectra in areas of different PL peak intensity in sample A17 (a), sample A19 (b), sample A21 (c), and sample B135 (d). [P2]

In thick, fully relaxed layers [see Fig. 4.5(d)], the long-wavelength band dominates the PL spectra in the areas with low and medium intensity.

It is worth noting that the spectra recorded in the areas of the highest PL intensity have one more band peaked between the two bands indicated by vertical lines. Position of this band corresponds to that calculated under

assumption that the layer is fully relaxed but contains as much indium as in the underneath strained layer. We assume that, the layers with the thickness exceeding the critical thickness contain nanocolumn-like structures with relaxed lattice, In content as in the initial strained layer and the density of nonradiative recombination centers that is lower than in the surrounding background with relaxed lattice and higher In content. Existence of similar nanocolumn-like structures has been previously observed by transmission electron microscopy study of InGaN epilayers [65]. In our PL intensity mapping images (Fig. 4.4), these nanocolumns are seen as bright spots. Typical luminescence spectra from the top of the column and surrounding regions are presented in Fig. 4.6. Formation of such columns can be explained by changing the growth mode from 2D to 3D as the InGaN layer thickness increases beyond critical value [53].

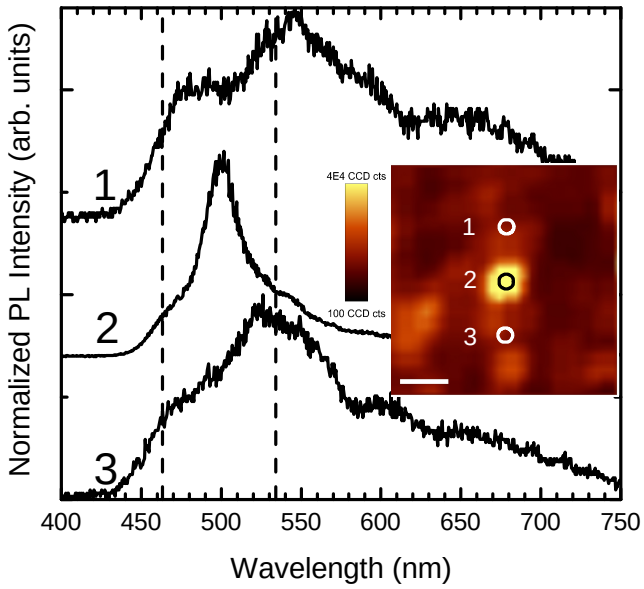

Fig. 4.6. Normalized PL spectra of sample B135 in areas of different PL intensity indicated in the spatial PL intensity distribution presented in the inset. The spectra are vertically shifted for clarity. The length of the white scale bar is 500 nm. [P2]

Study by AFM confirms the changes in surface morphology. The surface roughness increases from 0.9 nm for strained sample A17 to 47.3 nm for relaxed A23 layer. Typical AFM images of sample A17 and A23 are shown in Fig. 4.7. Coalescence of 3D-growth grains in thick layers (sample set B) results in a smoother surface again: the roughness in samples B90-B150 varies from

1.2 nm to 2.3 nm. Moreover, in the layers with the thickness only slightly exceeding the critical thickness, column-like structures might be spotted in the AFM image. The AFM image of sample A23, where the columns are most obvious, is presented in Fig. 4.7(a).

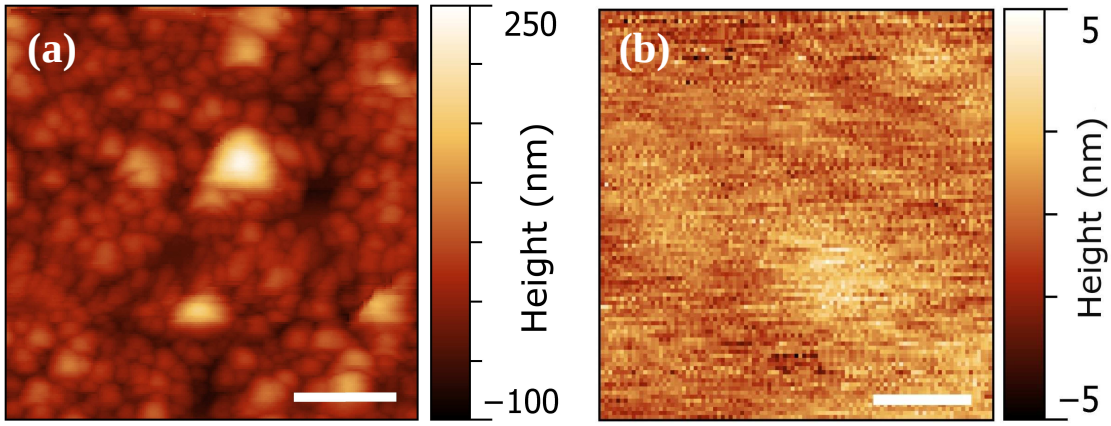

Fig. 4.7. AFM images of sample A23 (a) and sample A17 (b). The length of white scale bar is 500 nm. Note the scale change on Y axis in (b). [P2]

4.4. Short summary

In conclusion, transition from the initial strained layer to a subsequent relaxed layer, as the InGaN epitaxial layer is grown above the critical thickness, results in additional in-plane inhomogeneities of structural and optical properties due to the formation of the nanocolumn-like structures containing higher density of nonequilibrium carriers under photoexcitation. These nanocolumns have a relaxed lattice, In content as in the initial strained layer, a lower density of nonradiative recombination centers, and are surrounded by a background with relaxed lattice, higher In content, and higher defect density.

5. InGaN thermal annealing

5.1. Topic review

The yellow band (peaked at around 2.2 eV) is a common feature found in PL spectra of GaN layers [44]. Although the main research emphasis is placed on the band-edge luminescence, a broad and sometimes rather intense luminescence band peaked at 1.7–2.2 eV is also observed in PL spectra of InGaN epitaxial layers and multiple quantum wells (MQWs) [66–69]. As in the case of GaN, this luminescence band is assigned to shallow donor-deep acceptor pair recombination [44,67]. The deep acceptor is most often identified as gallium vacancies or its complexes with unintentional donors. On the other hand, the identity of the donor is hard to assign, since most of the donor impurities result in shallow energy levels [44].

The depth-profiling investigations of InGaN epilayers show that the defect-related luminescence comes mainly from the area of lower crystalline quality, close to the InGaN/GaN interface [70]. This is in consistence with observations of the intense yellow luminescence in GaN layers of poor quality [71]. The intensity of yellow luminescence can vary over a wide range and, as shown in Ref. [68], can even dominate over the band-edge emission of InGaN MQWs at room temperature. Poor optical properties of such MQWs were explained as a result of defects generated by strain relaxation of the well layers.

A direct link between yellow luminescence and defects in InGaN is determined using a scanning near-field optical microscope (SNOM). It was found that the most intense yellow luminescence was inside the V-shaped surface pits (V pits) of AlInGaN layers [72] and InGaN/GaN MQWs [43]. At the same time, the band-edge luminescence intensity at the V pits was weak. It was suggested that the defect-related emission inside the V pits is caused by deep gap states formed by gallium vacancies and impurity complexes, which are trapped at the side facets. This assumption was supported by transmission electron microscopy images, which showed defects gathered by the V pits.

The defect-related emission is undesirable for InGaN-based device performance. To suppress the defect-related emission, it is feasible to apply thermal annealing. In semiconductor manufacturing this process is often used to remove defects introduced by ion implantation. Previously, it was demonstrated that high temperature rapid thermal annealing is effective for improving the surface morphology and PL intensity of GaN layers [73]. The band edge luminescence intensity was increased after annealing in N_2 and Ar ambient, as compared to as-grown sample. At the same time, yellow luminescence decreased in the N_2-ambient annealed sample but increased in the Ar-ambient annealed sample. This suggests that additional defect levels were created during annealing in Ar, while N_2 ambient suppressed formation of the defects. Furthermore, annealing has been reported to have a significant influence on the structure of InGaN MQWs and epilayers [69,74,75]. InGaN epilayers tend to roughen upon annealing at temperatures above 700 °C. At annealing temperatures higher than 950 °C, indium loss from the layer surface is reported [76]. It was also found that indium desorption increases with increasing temperature and annealing duration [77].

Laser annealing is an alternative to thermal treatment. It may be advantageous due to its fast increase of temperature, controllable area of affection and much shorter annealing duration. Pulsed laser irradiation of Si-doped GaN layers caused a decrease in the intensity of the yellow band and an increase in the intensity of the band-edge luminescence [78]. These changes are similar to those observed after annealing in N_2 atmosphere and explained by a decrease in nitrogen vacancy concentration during annealing.

In section 5.2, we study the peculiarities of the photoluminescence (PL) spatial distribution in indium-rich InGaN epitaxial layers by using confocal microscopy. To reveal the features under study, epilayers with strong defect-related luminescence were selected and both the band-edge and defect-related luminescence bands have been studied. The dynamics of the two PL bands in $In_{0.21}Ga_{0.79}N$/GaN epilayer subjected to laser annealing was also investigated. Suppression of the defect-related emission by laser annealing was

demonstrated and the structural changes imposed by the annealing were studied by AFM and Auger electron spectroscopy (AES).

In an LED structure, the *p*-AlGaN electron blocking layer and the *p*-GaN hole transport layer are deposited on top of the active QW structure at elevated temperatures. This fabrication process affects the active structure of the LED acting as thermal annealing that can cause the changes in the potential distribution for carrier localization [79–84]. The changes in compositional fluctuations after thermal annealing have been previously observed in InGaN MQWs using transmission electron microscopy and cathodoluminescence measurements [79–83].

The effects of the high-temperature overgrowth of the *p*-type layers on emission properties have been studied in green-emitting InGaN/GaN QW LED structures by using conventional photoluminescence (PL) spectroscopy [85,86]. However, the conventional PL spectroscopy analyzes spatially-integrated spectra and does not allow assessing the properties of carrier localization directly. In section 5.3, confocal PL spectroscopy is used to get a better insight into the carrier localization peculiarities in such LED structures with different thicknesses of *p*-type layer grown on the top of the active QW structures at the same deposition temperature.

5.2. Influence of laser annealing on defect-related luminescence of InGaN epilayers

5.2.1. Samples and measurement techniques

The sample of a ~200 nm $In_{0.21}Ga_{0.79}N$ thin film with strong defect-related luminescence was used for study. The InGaN thin film was grown at 700 ^{o}C with 12 sccm in TMGa flow rate and 50 sccm in TMIn flow rate on a 2-μm GaN layer, which was deposited at 1000 ^{o}C on c-plane sapphire substrate. The sample was grown using metal-organic chemical vapor deposition (MOCVD) at the National Taiwan University.

At the Riga Technical University, small sections of the selected sample were annealed using the 2nd harmonic of the Q-switched Nd:YAG laser radiation (λ = 532 nm, pulse duration τ = 10 ns). The sample was sectioned into six ~900 μm-wide stripes, which were irradiated at different laser power densities ranging from 4.2 to 25 MW/cm^2. During the irradiation, the sample surface has been scanned using 20 μm steps by a laser beam focused into a 1 mm diameter spot. The irradiation has been performed at room temperature in ambient atmosphere.

The spatially resolved PL study in confocal mode has been performed using *WITec* microscope *Alpha* 300 coupled by an optical fiber with a *UHTS300* spectrometer followed by a thermoelectrically cooled CCD camera. A CW He-Cd laser emitting at 442 nm was employed for the excitation. The spatial PL distribution was studied at excitation power density of ~212 kW/cm^2. An objective with numerical aperture NA = 0.9 was used and ensured an in-plane spatial resolution of ~250 nm.

Changes in composition imposed by annealing have been studied by Auger electron spectroscopy (AES) technique (*Riber LAS*-3000 Auger spectrometer has been used). Profile of In, Ga and N contents in direction perpendicular to the surface has been studied by etching the surface under study by the beam of argon ions with kinetic energy of 3 keV and applying AES after every etching step. The Auger spectrometric measurements have been performed by J. Miškinis and dr. V. Kazlauskienė at the Materials Science Laboratory, Vilnius University.

5.2.2. Photoluminescence properties

Spectrally-integrated PL intensity mapping of 2×2 μm^2 area of $In_{0.21}Ga_{0.79}N$ epilayer is shown in Fig. 5.1(a). The image shows that the PL intensity is distributed highly inhomogeneously: a pattern of round-shaped areas of higher emission intensity is seen on the background of lower emission intensity (further referred to as dark and bright areas). The diameter of the bright areas is

typically around 250 nm (close to the limit of the spatial resolution in our experiments).

Figure 5.1(b) shows the PL peak wavelength mapping of the same area as in Fig. 5.1(a). White circles on Fig. 5.1(b) are drawn to indicate the areas of the most intense emission observed in Fig. 5.1(a). Although some shift towards short wavelength side for bright areas is distinguished, no clear correlation between PL intensity and peak wavelength is observed. Averaged PL bands from dark and bright areas peak at 523 nm [black solid line in Fig. 5.1(c) and 5.1(d)].

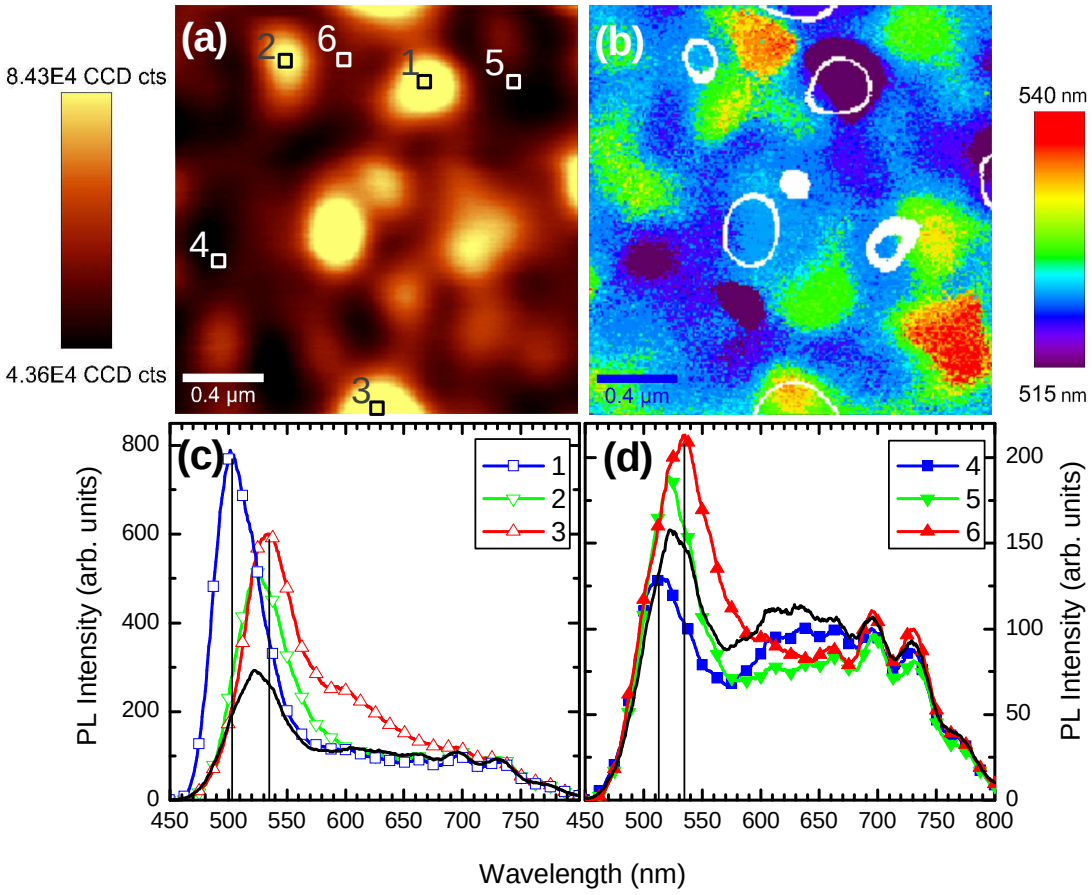

Fig. 5.1. Spectrally integrated PL intensity (a) and peak wavelength (b) mapping of $In_{0.21}Ga_{0.79}N$ layer and spectra of PL collected within spots in bright (c) and dark (d) areas (indicated). Solid black lines in (c) and (d) indicate averaged PL spectra in bright and dark areas, respectively. [P6]

Variation of PL spectrum in different sample surface areas has been studied by comparing the spectra collected from 80×80 nm^2 areas randomly selected in the bright and dark regions of the sample. Several characteristic spectra

obtained that way are shown in Figs. 5.1(c) and 5.1(d) for the bright and dark regions, respectively. All the collected PL spectra consist of two emission bands. The first band is peaked at ~530 nm and can be attributed to band-to-band optical transitions. The second band is centered at ~650 nm and is probably related to optical transitions involving defect-related levels. It is assumed that these levels are of similar origin as in GaN, i.e. created by donor impurities and gallium vacancies or its complexes with unintentional donors. This long-wavelength band is considerably broader than the short-wavelength one. Full widths at half maximum (FWHM) of these bands are ~66 nm and ~200 nm, respectively. The long-wavelength band is modulated [see Figs. 5.1(c) and 5.1(d)] by Fabry-Perot interference due to refractive index contrast at GaN/sapphire and the air/InGaN interfaces. Similar interference has been observed earlier in PL spectra from InGaN/GaN structures [87].

Two PL peaks observed in bright and dark areas of InGaN epilayer in Ref. [55] have been interpreted by inhomogeneous stress distribution in the epilayer. However, the difference in the peak positions of the bands (120 meV) observed in Ref. [25] is considerably smaller than that observed in our experiments (~480 meV), even by taking into account that the band gap difference between stressed and unstressed InGaN epilayers strongly increases with increasing In content [52]. Thus, we conclude that the low energy band observed in our sample is caused by defect-related recombination, as suggested in Refs. [66–69].

The intensity of the long-wavelength band remains almost the same in all the scanned area. Inhomogeneous intensity distribution is observed only for the short-wavelength band. Its intensity in the bright and dark areas varies by a factor of up to ~4. The shape and position of the long-wavelength band also shows no considerable spatial variations. Meanwhile, the peak position of the short-wavelength band varies approximately within the range from 500 to 538 nm irrespective of PL intensity.

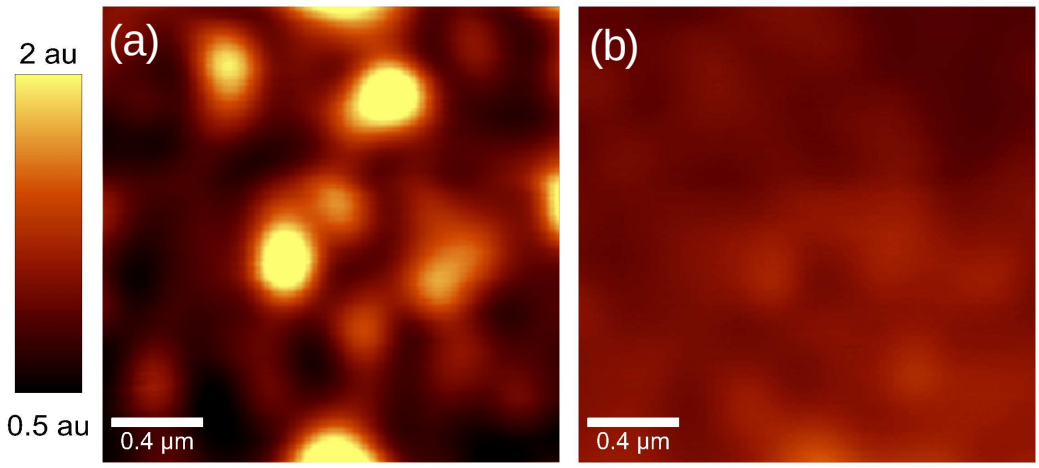

Fig. 5.2. Spectrally integrated PL intensity mappings of the same area of $In_{0.21}Ga_{0.79}N$ layer in different spectral ranges: 480 – 640 nm corresponding to band-to-band recombination (a) and 640 – 850 nm corresponding to defect-related recombination (b). Relative intensity range is the same for both mappings. [P6]

Since the PL spectra consisted of band-edge and defect-related luminescence bands, we compared the spatial distribution of these two bands by spectrally integrating emission separately in two spectral ranges: 450–640 nm for band-edge emission and 640–850 nm for defect-related emission. The resulting PL intensity mappings are shown in Fig. 5.2. To better reveal the variation of the PL intensity it was normalized by average intensity value of each spectral range. It can be clearly observed that the PL intensity of the defect-related band varies only within ~30%, while the band-edge emission is distributed considerably more inhomogeneously. The comparatively high fluctuations observed in the intensity distribution of band-edge luminescence [see Fig. 5.2(a)] can be attributed either to indium content fluctuations or inhomogeneous distribution of nonradiative recombination centers.

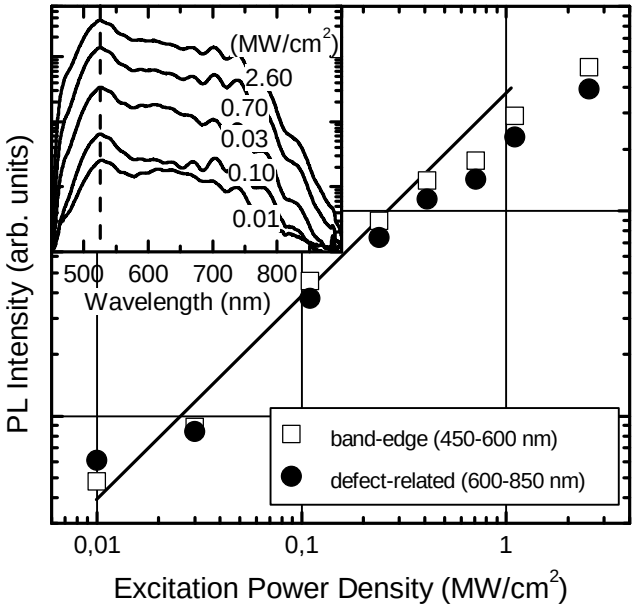

Fig. 5.3. Spatially and spectrally integrated PL intensity as a function of excitation laser power density in $In_{0.21}Ga_{0.79}N$ layer. Solid line shows linear PL intensity dependence. In the inset, spatially-averaged PL spectra at different excitation power densities are shown. [P6]

To gain more data on possible luminescence mechanisms, we studied the PL dynamics under different excitation power densities. Spatially-integrated PL spectra from 2×2 μm^2 area are shown in the inset of Fig. 5.3. The spectrum retained its structure and no obvious saturation of the defect-related emission intensity could be observed with increasing excitation. Only a small blue shift of the band-edge PL peak by 3-4 nm was observed. The spectrally-integrated PL intensity dependence on excitation power density is shown in Fig. 5.3 separately for band-edge and defect-related luminescence bands. Both dependences are very similar: they show a linear increase with excitation increase up to 0.5-1 MW/cm^2 and a sublinear increase under higher excitations. The observed linear dependence is consistent with recombination between localized electrons and holes. Carrier (exciton) localization due to indium content fluctuations is a peculiar feature in InGaN epilayers. The sublinearity at high excitation is probably caused by the gradual filling of the deepest localized states. This filling results in an increasing number of delocalized carriers that have higher probability to reach nonradiative recombination centers by hopping or tunneling and recombine nonradiatively there. The increase of defect-related emission intensity at increasing excitation is slightly slower than that for band-edge emission. This behavior can be explained by saturation of defect-related recombination centers, which is more pronounced in the bright areas. Note that the nearly linear excitation intensity dependence of the defect-related band

intensity up to the highest excitation power densities used points out to a large density of deep levels.

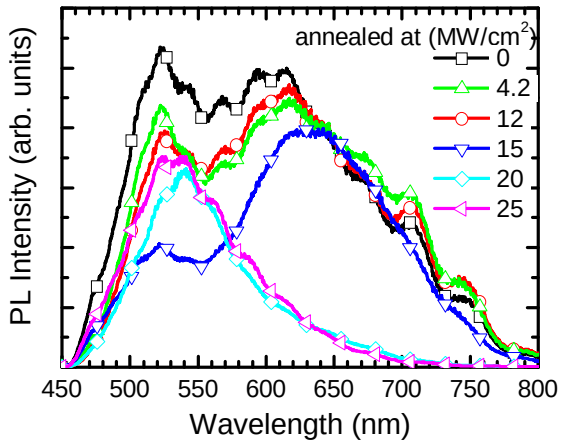

Fig. 5.4. Spatially integrated PL spectra of $In_{0.21}Ga_{0.79}N$ layer before (black curve) and after laser annealing at different power densities (indicated). [P6]

To study the possibility of reducing the defect-related luminescence intensity by laser annealing, sections of the sample under study have been subjected to laser radiation for the same exposition time but at different power densities. Spatially-integrated PL spectra from these sample sections are shown in Fig. 5.4. It is evident that annealing reduces the overall PL intensity (see Fig. 5.5, left axis). At low laser power density, laser annealing results in considerable suppression of band-edge PL. The ratio of the intensities of defect-related and band-edge PL is presented on the right axis in Fig. 5.5. Note that annealing at power densities above ~20 MW/cm^2 has a qualitatively different impact on PL spectrum: the defect-related band disappears and the band-edge luminescence intensity increases.

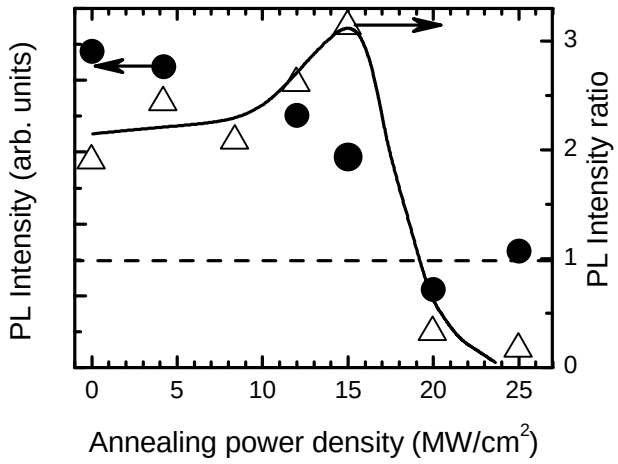

Fig. 5.5. Integrated PL intensity (circles, left axis) and ratio of intensities of defect-related and band edge PL in $In_{0.21}Ga_{0.79}N$ layer (triangles, right axis) dependences on annealing laser power density. Black solid line is shown as a guide for an eye. [P6]

Such an abrupt change in PL spectrum is probably caused by certain structural transformations inflicted by annealing laser radiation. AFM images presented in Fig. 5.6 evidence a

significant roughening of the surface by formation of bumps having predominantly 100 nm in diameter and 100 nm in height.

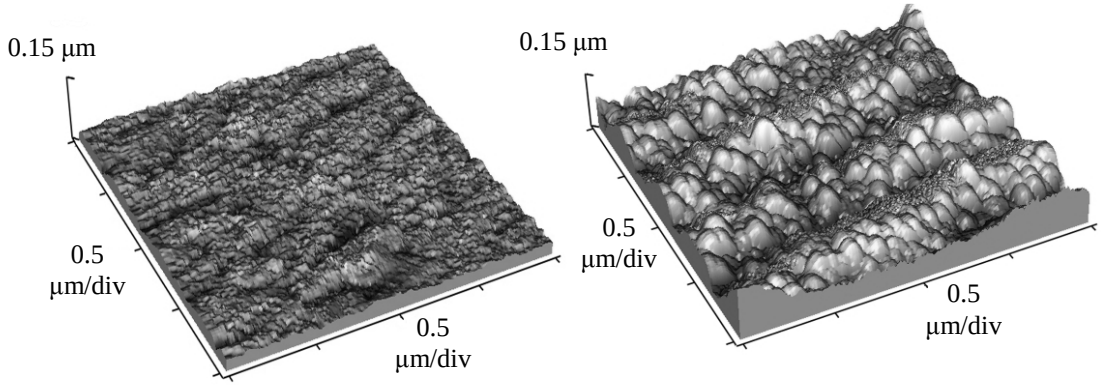

Fig. 5.6. Three-dimensional AFM images of $In_{0.21}Ga_{0.79}N$ surface before (a) and after (b) annealing at power density of 25 MW/cm^2. [P6]

5.2.3. The variation of In and Ga content in annealed compound

Influence of the annealing on composition of the epilayer has been further investigated using Auger electron spectroscopy (AES). To avoid the influence of surface, which was contaminated by adsorbed atoms, a thin surface layer (30 nm) was removed by argon ion etching before comparative AES experiments. No detectable changes in InGaN composition were observed in the sample sections annealed at low laser power densities, however, increase in indium and decrease in nitrogen concentrations were detected in sections subjected to irradiation at power densities below 15 MW/cm^2.

To compare annealed and as-grown (unannealed) areas, another annealing experiment was performed. The laser beam has been focused into a spot of 0.3 mm in diameter. After annealing, an AES scan across the spot and a part of unannealed surface on both sides of the spot was performed. The result for a spot subjected to annealing by 5 laser pulses at ~20 MW/cm^2 is presented in Fig. 5.7. Note that the concentrations plotted on vertical axis in Fig. 7 represent only relative values. The absolute signal values in AES experiments are affected by the escape depth of Auger electrons emitted by atoms of different

kind (~1.8 nm for Ga, ~1 nm for In and N). A few important features should be noticed: i) nitrogen content in an annealed spot increases; ii) the spot is depleted in indium; iii) the indium content in the annealed spot decreases significantly with increasing depth from the layer surface.

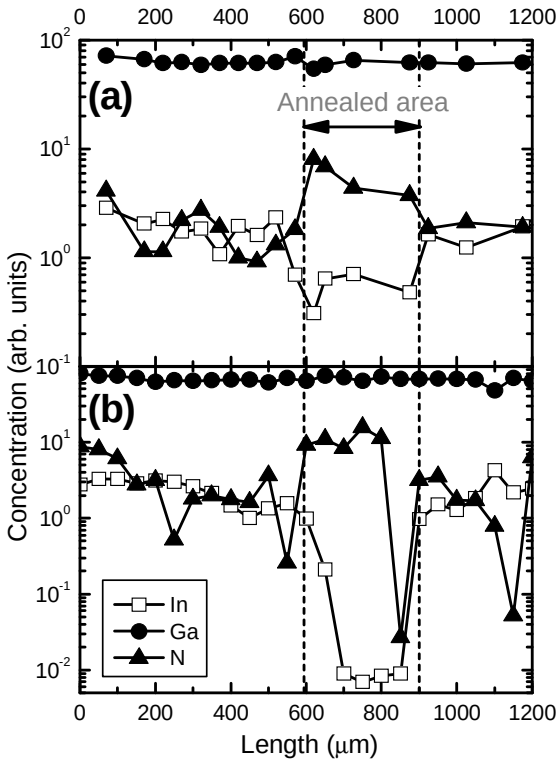

Fig. 5.7. Spatial distribution of In, Ga, and N content across a spot subjected to laser annealing. Data are obtained using Auger electron spectroscopy after ion etching of 30 nm (a) and 100 nm (b) of the upper layer of the InGaN sample. The arrow marks the annealed area. [P6]

It has been demonstrated previously that laser irradiation might enhance the surface atom migration and improve the layer crystalline quality [88]. This effect is also utilized in laser-assisted metalorganic vapor-phase epitaxy [89]. Our results of laser annealing possibly correlate also with the observation of the redistribution of In atoms under thermal annealing with the loss of indium-rich material by evaporation and, as a result, decrease in indium content [75]. Note that In-N bonds begin decompose at temperatures above ~650 ^{o}C [90] that can be easily reached at laser power densities used in our experiment. Thus, heating of the sample surface under laser annealing should enhance desorption of In atoms from InGaN layer surface and, consequently, result in indium depletion of the annealed spot. This explains AES results illustrated in Fig. 5.7 showing decrease of In content in an annealed spot.

5.2.4. Laser-induced thermogradient effect in structural rearrangement of InGaN

Summarizing the most distinct features of laser annealing of InGaN layers with strong defect-related luminescence we can conclude that the annealing at laser power densities exceeding certain threshold results in a decrease of indium content. This effect is evident on the sample surface, but becomes more pronounced deeper in the InGaN layer [compare Figs. 5.7(a) and 5.7(b)]. Vanishing of defect-related emission is simultaneously observed. The effect of In redistribution can be explained by taking into account the peculiarities of pulsed laser annealing, in particular, nonhomogeneous heating of the sample: the layers near the surface are heated to a higher temperature in comparison to the bulk of the crystal. In this case, the model of thermogradient effect (TGE) [91] can be applied. According to this model, the atoms with bigger effective radius in comparison to host atoms drift along temperature gradient towards the higher-temperature region, whereas the atoms with smaller dimensions drift to the opposite direction. In case of InGaN compound, In has the biggest radius, and N has the smallest one. This is completely in line with the observed space distribution of In and N atoms after laser annealing of InGaN layer.

It should be noted that laser annealing might result in healing of Ga vacancies, which, possibly, are a part of the defect complexes responsible for defect-related luminescence [43,67]. Thus, suppression of the defect centers responsible for the radiative recombination leading to sub-bandgap emission, which is parasitic to the band edge emission in light emitting devices, might be achieved by laser annealing.

5.2.5. Short summary

In conclusion, our spatially-resolved photoluminescence study of laser-annealed InGaN samples with strong defect-related luminescence reveals that

the defect-related luminescence exhibits no considerable spatial variations, while the band-edge luminescence has inhomogeneous spatial distribution, possibly, due to inhomogeneous In contribution or strain variations. We demonstrate that the defect-related emission in InGaN epilayers can be suppressed by laser annealing at power densities high enough to cause redistribution of In atoms. The effect is demonstrated in an InGaN epilayer exhibiting strong defect-related emission, but might be important to suppress the undesirable carrier recombination channel in high-In-content InGaN epilayers acting as active layers in LEDs and laser diodes.

5.3. Unintentional annealing of the active layer in the growth of InGaN/GaN QW LED structures

5.3.1. Samples and measurement techniques

The samples under investigation were grown and provided by the National Taiwan University. The samples under investigation had different layers deposited above the active MQW layer. The samples were grown on c-plane sapphire substrate using metal organic chemical vapor deposition. In each sample, five periods of QWs consisting of a 2.6-nm-thick InGaN well layer and a 12-nm-thick GaN barrier layer deposited at 670 and 820 ºC, respectively, were grown after the deposition of 2-µm *n*-GaN layer at 1100 ºC. In the reference sample (sample F), no additional layers were grown on the top the upper GaN barrier layer. In sample E, a 20 nm-thick *p*-$Al_{0.2}Ga_{0.8}N$ electron blocking layer was deposited on the top of the QW structure at the temperature of 960 ºC for growth duration of 25 s after a temperature ramping from 820 to 960 ºC within 140 s and temperature holding for 30 s under nitrogen flow. In samples D, C, B, and A, a 30, 60, 120, and 180 nm-thick *p*-GaN layer, respectively, was added on the top of the *p*-$Al_{0.2}Ga_{0.8}N$ layer at the growth temperature of 960 ºC after temperature holding for 120 s. The *p*-GaN growth durations for samples D, C, B, and A were 130, 260, 520, and 780 s, respectively. After the growth, the sample temperature was ramped down to room temperature within 35 min. No *in situ p*-type activation process was applied to any sample.

The QW widths (2.6 nm) and indium composition (22%) were estimated from the X-ray diffraction (XRD) measurements.

The spatially resolved PL study in confocal mode has been performed using *WITec* microscope *Alpha* 300. A CW He–Cd laser at 442 nm was employed for PL excitation. The PL excitation power density was ~ 12 kW/cm^2. Scans were performed over an area of 10×10 mm^2 with a step size of 50 nm to give an image of 200×200 pixels.

5.3.2. Statistical analysis of PL mapping images

Figure 5.8(a) shows the PL spectra spatially integrated over an area of $10\times10\ \mu m^2$ for samples A to F. The PL excitation power The PL intensities in samples B and C were by a factor of ~4 higher, than those in the other samples under study. The peak wavelengths of the PL bands in samples B and C are significantly blue-shifted from those in the other samples. The spatially-integrated PL spectra of all samples are broad, with the spectral full-widths at half-maximum (FWHMs) ranging from 165 to 200 meV. This is an indication that the spatially-integrated spectra are a superposition of PL spectra arising from sites with different effective band gap. The spatial distributions of PL intensity for samples A-F are shown in Fig. 5.8(b). Along with the PL intensity mappings, the corresponding mappings of spectral peak position and FWHM were also obtained (not shown here). The statistical data calculated from all the mappings are listed in Table 5.1.

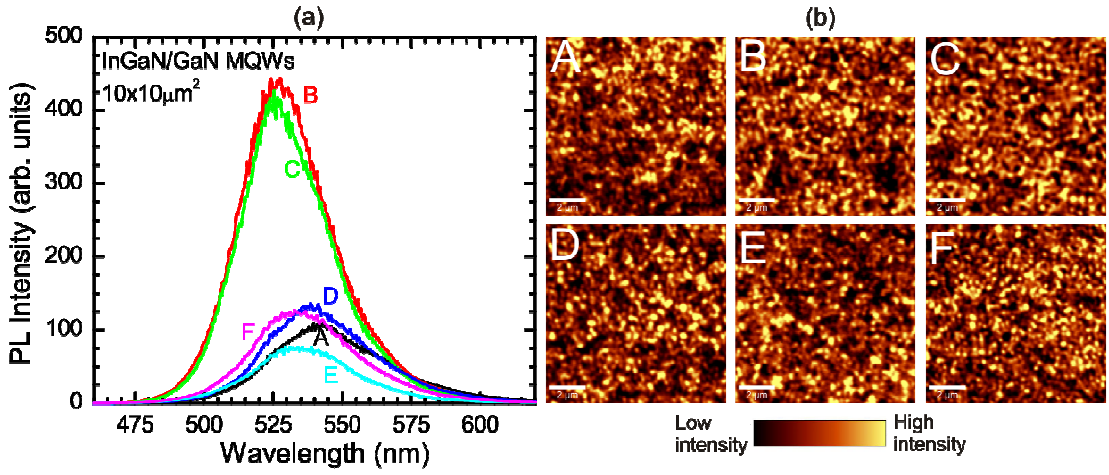

Fig. 5.8. Spatially-integrated PL spectra of samples A-F (a) and spatial distribution of PL intensity in each of the samples (b). [P3]

The mappings shown in Fig. 5.8(b) reveal a highly inhomogeneous PL intensity distribution: a pattern of round-shaped areas of a higher emission intensity on the background of a lower emission intensity (bright and dark areas, as referred to thereafter in the text below) can be clearly observed for all the samples. The typical dimension of the bright areas is around 250 nm (close to the limit of the spatial resolution in our experiments). Except the absolute

PL intensity, the mappings look very similar among the samples under study. The coefficient of intensity variation (the standard deviation divided by the mean value) varies very little, from 0.25 to 0.28 (see Table 5.1).

The point-to-point PL peak wavelength variations are rather small (e.g., the standard deviation is 4.8 nm, i.e., 21 meV in sample F). However, they are sample dependent: decreasing first from ~21 meV in sample F to ~9 meV in sample C, and then increasing up to ~14 meV in sample A. All the samples, except B and C, exhibit a weak positive correlation between the peak wavelength and the peak PL intensity, with the Pearson's product-moment correlation coefficient varying from 0.10 to 0.20. Meanwhile, no correlation was observed in samples B and C (the Pearson coefficient is negative and small, –0.09 to –0.06).

Table 5.1 Data of the structure and statistical parameters of the confocal PL scans shown in Fig. 1 of the InGaN/GaN QW LEDs under study.

Sample	A	B	C	D	E	F
p-AlGaN thickness (nm)	20	20	20	20	20	0
p-GaN thickness (nm)	180	120	60	30	0	0
PL intensity mean (arb. u.)	9.5	32.4	29.6	10.9	6.2	10.5
Intensity standard deviation (arb. u.)	2.7	8.7	8.1	3.0	1.9	2.6
Intensity variation	0.29	0.27	0.28	0.28	0.27	0.25
Peak wavelength mean (nm)	541.6	526.4	525.6	538.9	533.7	532.7
Peak wavelength deviation (nm)	3.4	3.2	2.1	2.2	4.7	4.8
FWHM mean (meV)	187	165	162	176	166	175
FWHM standard deviation (meV)	21.5	14.8	14.4	16.6	13.9	17.1
Peak wavelength-to-peak intensity Pearson's correlation coefficient	0.10	-0.09	-0.06	0.20	0.14	0.13
Peak wavelength-to-FWHM Pearson's correlation coefficient	0.21	0.35	0.33	0.23	0.08	0.20

Even though the spatial variations of the PL spectral peak position are not large, the single-point spectra (collected from an area of 200×200 nm^2 in our experiment) are rather broad, with the FWHM ranging from 144 to 225 meV for the samples under study. The large FWHMs of the PL spectra from the individual points in the mappings indicate that the confocal spectra are the superposition of PL spectra arising from small-spatial-scale localization areas not resolved in the confocal measurements with the spatial resolution of ~240 nm. This implies that the samples under study have a double-scaled potential profile: the larger areas (hundreds of nanometers to a couple of

micrometers) are revealed by the confocal measurements, while the smaller areas (probably, a few of nanometers in size) manifest themselves through the inhomogeneous broadening of the confocal spectra. Such a smaller area corresponds to an indium-rich nano-cluster, which is responsible for the strong carrier localization behavior in such a QW structure [79]. The double-scaled potential profile model has been suggested to explain the peculiarities of exciton dynamics in AlInGaN materials [21], and has been successfully applied to InGaN/GaN QWs [22]. A similar approach to analyze PL mappings has recently been used to study carrier localization in InGaN/GaN QWs [92] and AlGaN epilayers [93].

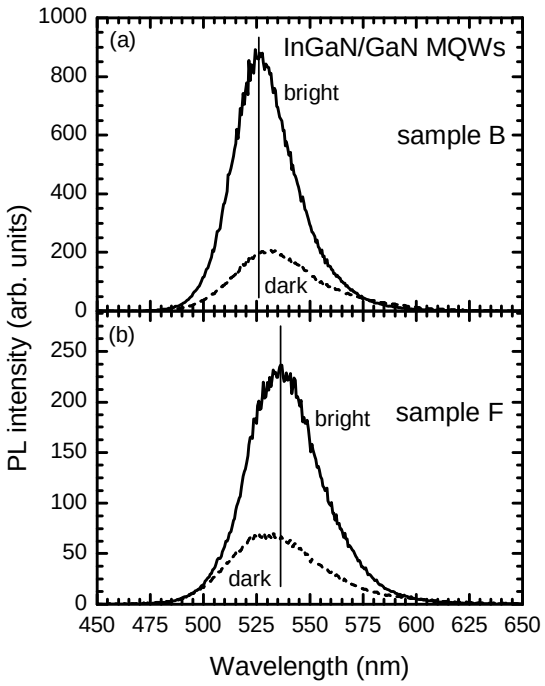

Fig. 5.9. PL spectra from the bright (solid lines) and dark (dashed lines) areas in samples B (a) and F (b). Vertical lines indicate the peak positions of the spectra from the bright areas. [P3]

To gain more information about the possible mechanisms of the inhomogeneous PL intensity distribution, we analyzed the PL characteristics in the bright and dark areas separately. Several PL spectra from the bright and dark areas in samples B (the sample having the highest spatially-integrated intensity) and F (the sample without any *p*-type layer) are shown in Fig. 5.9. The peak wavelengths in the bright areas are slightly blue-shifted compared to those in the dark areas in sample B, while this trend is reversed in sample F. Such a behavior is consistent with the calculated correlation coefficients between the peak wavelength and the peak PL intensity in the two samples.

We select 4000 pixels (10% of the total number) exhibiting the lowest intensity and 4000 highest-intensity pixels for each sample, and study their

average PL characteristics. Figures 5.10 and 5.11 present these characteristics for all six samples as a function of the total *p*-type layer thickness.

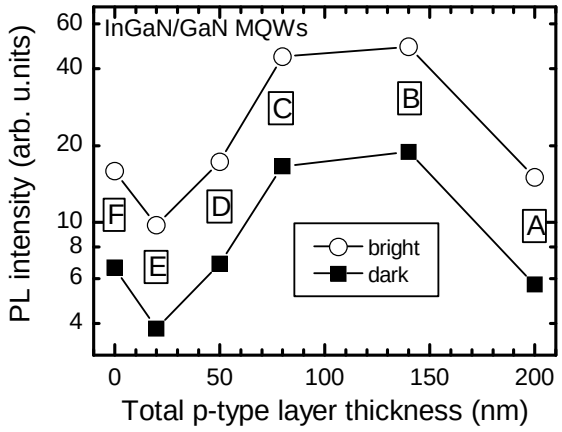

Fig. 5.10. Dependences of the PL intensities in the dark (solid rectangles) and bright (open circles) areas. The points correspond to samples A to F (indicated). [P3]

Several interesting features can be noticed when analyzing the sample characteristics in detail. First, the average PL intensity in the dark areas of samples B and C is higher than the average PL intensity in the bright areas of other samples under study [see Fig. 5.10(a)]. Second, the spectral peak position first red-shifts, blue-shifts, and then red-shifts again, as the total p-type layer thickness is increased [see Fig. 5.11(a)]. This trend is true for both dark and bright areas. Third, as the total *p*-type layer thickness is increased up to ~150 nm, the difference between the average spectral peak positions in the dark and bright areas decreases, but starts increasing afterwards [see Fig. 5.11(a)]. Finally, the FWHM of the PL bands in samples B and C are the smallest among the samples under study. This behavior is more pronounced in the bright areas [see Fig. 5.11(b)].

Since the average indium content and well width in samples A-F were estimated to be almost the same, the observed differences in spatially-integrated emission wavelength and PL intensities should be caused by the changes of material structure in the active region. Annealing of the active region during the deposition of the *p*-type layer at 960 ºC and the variation in the QCSE due to increasing thickness of the *p*-type layer can be pointed out as the main factors influencing the PL results.

5.3.3. Concurrent influence of thermal annealing and QCSE on PL properties

The thermal annealing process may change the potential depth and density of localized states resulting in either stronger or weaker carrier localization [79–84]. Two models are usually suggested to explain the thermal annealing effect. According to the first model, upon thermal annealing, a spinodal decomposition dominates the process of relaxing the strain energy built in the well layers. In this process, the "up-hill" diffusion results in accumulation of indium towards the core of In-rich sites and forms more inhomogeneous structures [81–83]. Recently, this model has been used to explain the macroscopic PL results in similar InGaN/GaN QWs without any over-grown p-type layer but subjected to thermal annealing of different durations [86]. However, the formation of the nano-clusters with even higher indium content on the background with reduced indium content would increase the potential variation on small spatial scale, thus increasing the FWHM of the single-pixel PL spectra. This is in contrary to our observation [see Fig. 5.11(b)]. The second model proposes that during thermal annealing, the out-diffusion of the indium-rich phase into the surrounding matrix and the inter-diffusion at the InGaN/GaN heterojunctions occur simultaneously, which results in more homogeneous composition distribution [79,80]. The more homogeneous indium distribution flattens the small-scale potential profile, and concurrently reduces the large-scale inhomogeneities. This results in a peak wavelength blueshift, decreasing the spectral peak energy difference between the dark and bright areas, decreasing the variation of the spectral peak position, and decreasing the FWHM of both spatially-integrated and single-pixel PL spectra. The last three features are observed in our experiments (see Fig. 5.11 and Table 5.1), while the peak position shift is probably additionally affected by the QCSE, as discussed below.

Thermal annealing might cause not only the redistribution of indium atoms but also might introduce additional points defects [77] or generate dislocations

[84] in the active region. However, these effects are not in consistence with our observation that the PL intensity in the dark areas in samples B and C is comparable or higher than the PL intensity in the bright areas of the rest of the samples under study. The overall increase of PL intensity is consistent with the defect healing effect [75, P6].

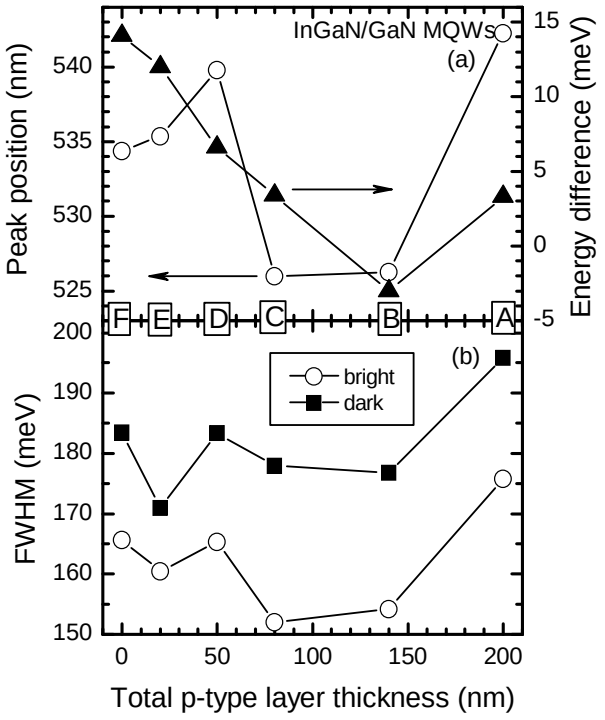

Fig. 5.11. Dependences of the energy difference between the dark and bright areas (solid triangles) and the spectral peak position in the bright areas (a) and the spectral FWHM (b) in the dark (solid rectangles) and bright (open circles) areas on the total *p*-type layer thickness. The points correspond to samples A to F (indicated). [P3]

The increase of *p*-type layer thickness can increase the strain and enhance the piezoelectric field and, hence, the QCSE in the QWs [94]. The increasing piezoelectric field causes a redshift of the PL band peak wavelength. The simulations of the built-in field in the structures under study show that, indeed, the piezoelectric field increases with increasing *p*-type layer thickness, however, the field saturates when the *p*-GaN layer thickness is larger than 60 nm [86].

The observed experimental results can be explained by the concurrent influence of thermal annealing and QCSE. As the *p*-type layer thickness and, consequently, the thermal treatment time increase (samples F to D), the annealing heals a part of defects acting as nonradiative recombination centers and facilitates a more homogeneous distribution of composition in the QWs. As a result, the PL intensity increases due to the reduced influence of nonradiative recombination, while the PL band blueshifts and becomes slightly narrower. Also, the differences in band peak positions and in PL intensities of the bright and dark areas decrease due to smoothening of the potential

fluctuations as indium distribution becomes more homogeneous. The smoothening of the potential profile blueshifts the PL band, while the simultaneous increase of QCSE due to increasing p-type layer thickness causes a redshift. The overall redshift of the band in samples from F to D might be interpreted by overwhelming influence of QCSE.

As the p-type layer thickness is further increased (samples D to B), the QCSE effect saturates, and the PL band properties become determined mainly by the potential profile smoothening due to the thermal annealing. Thus, the PL band peak position blueshifts, while the difference between spectral peak positions in the bright and dark areas further decreases. Moreover, the reduction of the potential fluctuations results in redistribution of photoexcited carriers among the localized states. The enhanced carrier mobility by hopping via localized states facilitates accumulation of the carriers in areas with lower in-plane average potential (bright areas). The higher carrier density in the bright areas results in more efficient screening of the built-in field and blueshifts the PL band even above its position in the dark areas [see Fig. 5.11(a)].

The opposite tendency in the variation of these parameters observed in sample A with the thickest *p*-type layer can be explained by smoothening of both large-scale and small-scale potential fluctuations. Smoothening of the small-scale potential fluctuations results inmore extensive moving of the carriers across the crystal, a higher probability for them to reach nonradiative recombination centers, and in a lower overall PL intensity. Moreover, smoothening of the large-scale potential fluctuations diminishes carrier accumulation in bright areas. As a result, the internal electric field becomes less screened, and the PL band position redshifts back to its position observed in sample D.

5.3.4. Short summary

In conclusion, the variation of PL characteristics with increasing thickness of *p*-type layer in InGaN/GaN QW LED structure is mainly caused by the thermal treatment occurring during the *p*-type layer deposition. This unintentional annealing of the active layer results in the smoothening of the potential fluctuations due to inhomogeneous indium distribution in the QWs. For thin *p*-type layers up to approximately 150 nm, the annealing improves the emission properties of the structure but becomes detrimental for thicker *p*-type layers due to the delocalization of a significant part of nonequilibrium carriers. The quantum confined Stark effect considerably influences the PL characteristics only in the structures with thin *p*-type layers up to approximately 60 nm and becomes unimportant due to the saturation of the internal field variation as the *p*-type layer thickness is further increased.

6. Spatial distribution of emission properties due to inhomogeneous defect distribution in InGaN light-emitting diode structures

6.1. Topic review

Localization and inhomogeneous spatial distribution of nonequilibrium carriers (excitons) in InGaN in blue and white light emitting diodes (LEDs) and blue laser diodes play a crucial role in the light emission of InGaN epilayers and heterostructures [95] but peculiarities of these processes are still not fully understood.

Cathodoluminescence (CL) [23,25,96,97], μ-PL [33,98,99], confocal spectroscopy [35,100,101], and scanning near field optical microscopy (SNOM) [36,40,102,103] reveal inhomogeneous photoluminescence intensity distribution in InGaN epilayers and QWs. Many publications [19,102,104,105] point out to the well width fluctuations as the main origin of inhomogeneous spatial PL distribution in InGaN QWs, and dislocations are claimed to have a significant effect on the local emission efficiency [40,106]. Localization of excitons on a nanometer scale might be also caused by the localization of the hole wave functions around indium in randomly formed In-Ga-In chains, as theoretically predicted for cubic InGaN [107].

In InGaN quantum wells (QWs), optical transitions and carrier dynamics are affected by the quantum-confined Stark effect (QCSE) due to the built-in electric field that can be screened by nonequilibrium carriers [35,108] and by filling-in of the localized states. Both the effects often have a similar effect on PL characteristics of the InGaN QW.

In this chapter, the spatial distribution of photoluminescence in LED structures with InGaN multiple quantum wells (MQWs) as an active region is studied. PL spectroscopy in the confocal mode was employed and revealed unusual features of the inhomogeneous PL spatial distribution. The strongly pronounced PL features we observe in our study cannot be interpreted as caused by localization and field-induced effects.

6.2. Samples and measurement techniques

The green LED structure under study was grown and provided by Sensor Electronic Technology, Inc. The sample was grown on the *c*-plane sapphire by metal-organic chemical vapor deposition. Trimethyl indium (TMI), trimethyl gallium (TMGa) and ammonia (NH_3) were used as In, Ga and N sources, respectively. The structure consisted of a 0.3 μm thick AlN buffer layer, 3 μm thick Si-doped *n*-GaN layer, InGaN compliance layer, 5-period InGaN/GaN MQW active layer, 20 nm thick *p*-AlGaN electron block, and 0.2 μm thick *p*-type contact layer. The active layer contained 2 nm-wide $In_{0.27}Ga_{0.73}N$ wells and 5 nm-wide GaN barriers.

The PL intensity mapping and the study of spatial variations in PL spectra on submicrometer scale have been performed using *WITec* confocal microscope *Alpha 300 S*. Objective with numerical aperture NA = 0.9 was used and ensured an in-plane spatial resolution of ~250 nm. For spectral resolution, the microscope was coupled by an optical fiber with a *UHTS300* spectrometer followed by a thermoelectrically cooled CCD camera. A CW He-Cd laser emitting at 442 nm was employed for the excitation. All the experiments have been carried out at room temperature.

The excitation power density dependence of the relative quantum efficiency of spatially-integrated PL in a wide dynamic range have been carried out under quasi-steady-state excitation by the third harmonic of Q-switched YAG:Nd laser radiation (3.49 eV).

6.3. Negative correlation between PL intensity and spectral band position in InGaN LED structures

The mapping images of spectrally integrated PL intensity are presented in Fig. 6.1(a). The figure reveals a strongly inhomogeneous spatial distribution of the emission intensity in the MQW plane: regions of stronger emission are evident on the background of lower emission intensity. The bright spots in the

mapping image typically have a round shape of ~250 nm in diameter (close to the spatial resolution of the confocal microscope used). The PL intensity in the bright spots exceeds that in the background by a factor of up to 8.

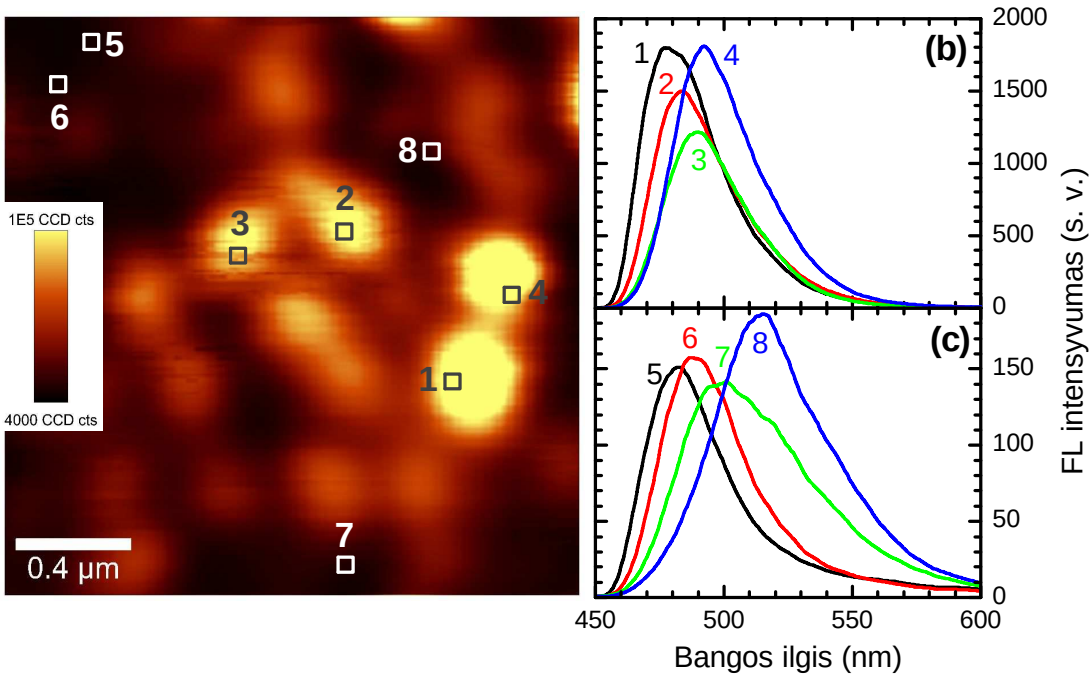

Fig. 6.1. Typical PL intensity mapping ($2\times2\ \mu m^2$) image of InGaN-based LED structure (a) and several PL spectra taken from spots indicated on the map in bright (b) and dark (c) areas. [P5]

The spectral PL distribution in the MQW plane was studied by comparing the emission spectra in small spots (50×50 nm, 5×5 pixels) picked up from the regions of low and high emission intensity (dark and bright areas, as referred to further in the text). Several of these PL spectra are presented for bright and dark areas in Fig. 6.1(b) and 6.1(c), respectively. The spots, from which the corresponding spectra were acquired, are marked and labeled in the mapping images [Fig. 6.1(a)]. A considerable scattering in intensities and peak wavelengths of the PL bands acquired from different spots in the bright and dark areas is quite evident. The resulting FWHM of the spatially-integrated PL band (measured at high excitation intensities when a single band prevails) is 38 nm in bright and 51 nm in dark areas.

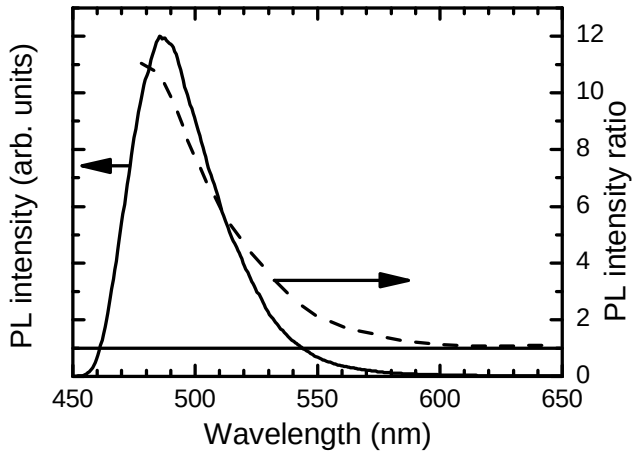

Fig. 6.2. Spatially-integrated PL spectrum in bright areas (solid curve) and spectral distribution of ratio of PL intensity spatially integrated in bright and dark areas (dashed curve). [P5]

The spatially-integrated dark area band peak is redshifted by 10 nm in respect to the band position in the bright areas. The comparison of the PL bands recorded from different spots shows that this redshift and broadening of the spatially-integrated PL band in the dark areas is caused by a lower intensity of PL emitted from spots corresponding to shorter wavelengths, while the emission intensities in the long wavelength region are similar in the dark and bright areas (see Fig. 6.2).

To gain more data on possible mechanisms of the inhomogeneous PL intensity distribution, we studied the PL properties of our sample at different nonequilibrium carrier densities. Figure 6.3 presents the PL spectra measured in a dark area at different excitation power densities. The spectrum is basically dominated by a single band, which is peaked at ~500 nm and shows a considerable band shift with increasing excitation. In addition to the prevailing band, another PL band [peaked at considerably longer wavelengths (~560 nm)] was observed in the dark areas, but its intensity saturated with increasing excitation. This PL band probably involves defect-related states. No long-wavelength band was observed in the bright areas.

The excitation power density dependences of the peak position of the main PL band for the bright and dark areas are compared in Fig. 6.4(a). The band peak in the dark areas gradually blueshifts by ~25 nm when the excitation power density is increased from 4×10^{-3} to 2.4 MW/cm^2. A striking feature is that the band peak in the bright areas at low excitation power densities is at a shorter wavelength than that in the dark areas. With increasing excitation

intensity, the PL band in bright areas first blueshifts slower than that in dark areas but the shift rate becomes similar in both areas at high excitation intensities.

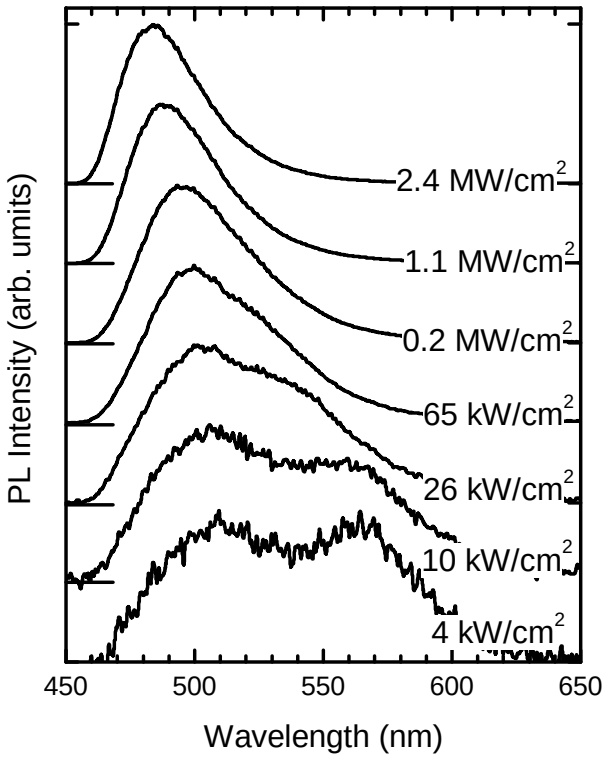

Fig. 6.3. PL spectra in dark area at different excitation power densities. The spectra are normalized and shifted along vertical axis for clarity. [P5]

The excitation power density dependences of the spectrally integrated PL intensity in bright and dark areas are presented in Fig. 6.4(b). The dependence is linear at low excitation, but becomes superlinear at elevated excitation power densities. To study the PL efficiency dependence on excitation power density in a wider dynamic range, experiments have been performed under quasi-steady-state pulsed excitation (pulse duration 20 ns) [Fig. 6.4(c)]. Note that the photon energy at the quasi-steady-state pulsed excitation (3.49 eV) was high enough to excite the 5 nm-wide barriers, while in the CW excitation (photon energy 2.8 eV) only the 2 nm-wide quantum wells were excited. Thus, at the same excitation power density, the expected carrier density under the pulsed excitation is larger than that under the selective excitation approximately by a factor of 3. Moreover, the small excess energy of the photoexcited carriers might also diminish the spillover effect, which probably is one of the mechanisms causing the efficiency droop effect [109]. Comparison of Fig. 6.4(b) and 6.4(c) shows that the droop is observed at a higher carrier density than that achieved in our spatially-resolved experiments.

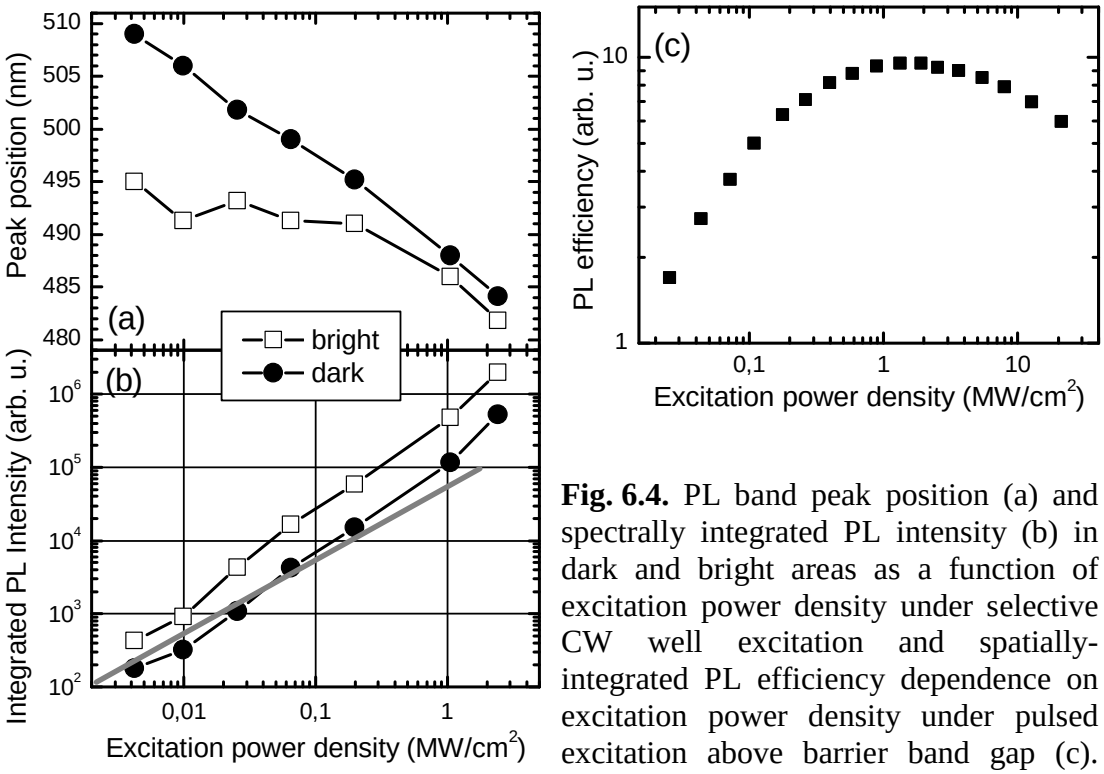

Fig. 6.4. PL band peak position (a) and spectrally integrated PL intensity (b) in dark and bright areas as a function of excitation power density under selective CW well excitation and spatially-integrated PL efficiency dependence on excitation power density under pulsed excitation above barrier band gap (c). Solid line in (b) shows a linear PL intensity dependence. [P5]

The PL band shift with increasing excitation intensity in InGaN QWs is usually explained by two effects: gradual population of the lowest localized states and screening of the built-in electric field. Both effects result in a blue shift of the PL band and their contributions are difficult to distinguish.

We calculated the energy levels in the quantum well with a built-in electric field by simultaneously solving the stationary Schrödinger equation and the Poisson equation describing the asymmetric space–charge distribution in the well. Using material parameters taken from [3] and approach suggested in [110] results in the built-in field at GaN/$In_{0.27}Ga_{0.73}N$ of 3.4 MV/cm. Such a field shifts the energy of the lowest optical transition by ~200 meV. The built-in field of 1.5 MV/cm, which is a typical low-bound value estimated for similar GaN/InGaN interfaces [111], results in a shift of ~60 meV. Carrier densities sufficient to cause a significant blue shift of the lowest optical transition due to screening of the built-in field are lower in wider QWs. In the 2 nm-wide well under study, a blue shift of 10% from the entire QCSE shift occurs at densities of ~2×10^{12} cm^{-2}. The estimation of the carrier density in our

PL experiments is obscured by uncertainty in the carrier lifetime, which locally depends on the carrier localization depth and on the carrier density. Assuming the lifetime to be 1 ns, the excitation power densities in our experiments (from 4 kW/cm^2 to 2.4 MW/cm^2) correspond to the carrier densities ranging from 2×10^{10} cm^{-2} to 10^{13} cm^{-2}. Thus, the faster blue shift of the PL band at the highest excitation power densities in our experiments should be influenced by the screening effect but the lowest excitation intensities used hardly imposes significant screening. This conclusion is supported by the excitation power density dependence of the PL intensity [see Fig. 6.4(b)], which is linear at a low excitation but becomes superlinear at the excitation power densities exceeding approximately 0.1 MW/cm^2. There is no return of the linear dependence, which is expected after the built-in field is completely screened. This might be an indication that the built-in field is not completely screened even at the highest excitation power densities used in our experiments. On the other hand, the superlinear growth of PL intensity at increasing excitation power density might also be expected due to the saturation of nonradiative recombination centers.

Localization and inhomogeneous spatial carrier distribution due to the fluctuations in indium content and/or well width definitely plays an important role in the samples under study. It is usually assumed that the deeper carrier (exciton) localization (corresponding to a lower energy of the photon emitted via radiative recombination in the localized states) results in a higher PL intensity due to decreased probability of carrier hopping and reaching nonradiative recombination centers. Thus, the inhomogeneous PL intensity distribution could be explained by inhomogeneous distribution of deep localized states. Contrary to this assumption, the PL peak position in the bright areas of the sample under study is higher in energy than in the dark areas. The Pearson's product-moment correlation coefficient of -0.2 indicates a negative correlation between the PL intensity and the peak wavelength.

The difference in $In_xGa_{1-x}N$ content with $x \approx 0.27$ corresponding to the PL band shift observed (~10 nm) would be rather small (of the order of $\Delta x = 0.01$) and hardly could cause the observed increase in PL intensity by a factor of 8 due to possibly higher structural quality in the areas with lower In content.

The bright spots could be interpreted as regions with narrower well width, where the blue shift of the PL band is stronger and the PL intensity is higher due to stronger overlap of the electron and hole wavefunctions. Though qualitatively consistent with experimental results, this effect is expected to be considerably weaker than observed. At low carrier density, the square of the wavefunction overlap for 1.75 nm wide well exceeds that for 2.25 nm well by a factor of two. This difference would actually be even lower due to stronger screening in the thicker regions, where a higher carrier density should be expected. Consequently, the increase in the overlap of electron and hole wavefunctions is insufficient to explain the intensity difference of up to the factor of 8.

The lower PL intensity in areas where emission occurs at longer wavelength might be also explained by an inhomogeneous spatial distribution of the built-in field: a higher field causes a larger PL band redshift due to QCSE and, hence, a smaller overlap of the electron and hole wavefunctions and, consequently, a smaller rate of radiative recombination and a lower emission intensity. However, according to our calculations discussed above, this effect cannot explain such a big difference in the PL intensity in the bright and dark areas. The difference of ~25 nm observed for PL band peak positions in bright and dark areas at low excitation power density [see Fig. 6.4(a)] corresponds to variation of the built-in field by ~30%. The built-in field of 3.4 MV/cm causes a decrease of the squared electron and hole wavefunction overlap in a 2 nm QW down to 25% of the value for a rectangle QW (with zero built-in field). A variation of the field by 30% results in a change by a factor of 1.5 in the PL intensity due to the overlap change, which is much smaller than the observed factor of 8.

6.4. Influence of inhomogeneous distribution of nonradiative recombination centers on intensity and spectral features of photoluminescence

We suggest that the inhomogeneous PL intensity distribution observed in the structure under study can be explained by an inhomogeneous distribution of nonradiative recombination centers, as previously reported in [P7]. The probability of nonradiative recombination is higher for the carriers (excitons) occupying the states with smaller localization energy. These excitons, which are responsible for the short-wavelength side of the PL band, have a higher probability to reach nonradiative recombination centers by hopping. Thus, the nonradiative recombination suppresses emission mainly on the high energy side of the PL band resulting in a redshift of the band. The higher is the density of nonradiative recombination centers, the stronger is the redshift. Thus, the PL band in the dark areas is at longer wavelengths than the band in the bright ones. This interpretation is strongly supported by the data presented in Fig. 6.2. As seen, the intensity is equal both in bright and dark areas at the long-wavelength tail of the PL band but the intensity in bright areas is progressively higher at the shorter wavelengths.

As the carrier density increases, more localized states become occupied. This effect results in a blue shift, which compensates the red shift caused by the nonradiative recombination centers. The blue shift due to the state filling is stronger in the spectral region corresponding to the tail of the density of the localized states and becomes less pronounced in the spectral region corresponding to a higher density of the states. The results presented in Fig. 6.4(a) are consistent with this interpretation: the blue shift of the PL band at increasing excitation power density is more pronounced in the dark areas. As discussed above, the overall blue shift, which is observed in the bright areas, should be influenced by screening of the built-in field.

The conclusion that the inhomogeneous PL spatial distribution is strongly affected by an inhomogeneous distribution of the nonradiative recombination centers is indirectly supported by the observation that the additional long-wavelength emission band is present in the dark but not in the bright areas. As shown in Ref. [71] for GaN, the densities of nonradiative recombination centers and the centers of radiative defect-related recombination (causing yellow luminescence) are correlated. Provided that a similar conclusion is valid also for InGaN, the presence of the long-wavelength PL band in dark areas is an indication that these areas contain also a higher density of nonradiative recombination centers. The unusual PL characteristics and their dynamics under increasing excitation power density are consistent with the assumption that this sample has inhomogeneous distribution of nonradiative recombination centers. This feature can be favorable for higher emission efficiency. In the areas with a lower density of nonradiative recombination centers, the carrier density is higher and screens the built-in field more effectively.

Spectrally-integrated PL intensity dependence on carrier density [see Fig. 6.4(b)] is the same in bright and dark areas but a higher excitation power density is necessary to reach the same carrier density in the dark areas due to a higher density of nonradiative recombination centers. The origin of the inhomogeneous distribution of nonradiative recombination centers is unclear. It is worth noting, however, that the structure under study contains 5 QWs. The spatial resolution in the Z direction (perpendicular to the layers) is 0.75 μm, i.e. includes all the QWs. Hence, the bright areas vertically coincide within ~250 nm in all five QWs. Otherwise, the image would be washed out, and no distinct bright areas of ~250 nm in diameter would be observed. Such a vertical alignment implies possible involvement of dislocations propagating vertically though the QWs. At dislocation density of 10^9 cm^{-2}, the 2×2 μm^2 sample area depicted in Fig. 6.1(a) should contain 40 dislocations on average. It can be expected that these dislocations concentrate in the dark areas and are absent in the bright areas.

6.5. Short summary

In conclusion, confocal microscopy revealed spots of a more intense photoluminescence (~250 nm in diameter) in green LED structures with $In_{0.27}Ga_{0.73}N$ MQWs as an active region. The spectral features in the dark and bright areas and dynamics of the photoluminescence characteristics under increasing excitation power density point out to an inhomogeneous distribution of nonradiative recombination centers that affects the carrier density distribution and screening of the built-in field in the QWs and leads to nonuniform emission intensity.

7. Enhancement of emission efficiency in InGaN quantum wells due to coupling with localized surface plasmons in Ag nanoparticles

7.1 Topic review

Light emitting diodes (LEDs) based on InGaN/GaN multiple quantum wells (MQWs) have been commercialized for many applications. However, good prospects for improvements in their performances still remain. The main current problems to solve are high nonradiative recombination, efficiency reduction at a high injection current density (the efficiency droop effect) [112], and low crystal quality for emitting at long wavelengths (in ”the green death valley”) [4].

The most straightforward approach for the enhancement of LED efficiency is decreasing the nonradiative recombination rate by improving the crystal quality. The optimization of growth conditions and buffer layers provide us with incremental but saturating improvement, while the epitaxial lateral overgrowth (ELOG) technique [113,114] and the replacement of sapphire substrate by low dislocation density GaN substrate [115] are more effective but still quite expensive.

Alternatively, LED efficiency can be increased by enhancing radiative recombination rate. The enhancement can be achieved by coupling the emitting dipoles in the QWs with surface plasmon polaritons (SPPs) induced on metal/dielectric interfaces [116,117] or with localized surface plasmons (LSPs) on metal nanoparticles (NPs) [118–120]. Surface plasmon (SP, including SPP and LSP) represents a quantum of the collective electron oscillations induced at an interface between metal and dielectric or semiconductor. Provided that the emission wavelength of the radiating dipoles in the QWs matches that of the SP resonance and the QWs are covered by metal structures containing SP and being in the proximity short enough for coupling via the near field, the radiating dipoles in the coupled QWs can transfer energy to SPs. The SP energy is subsequently radiated when the momenta of photon and SP are

matched. Momentum matching is granted either by the roughness of the metal surface or by a metal grating structure. Meanwhile, an LSP has zero momentum and can effectively radiate without any momentum matching mechanism. Thus, SP-QW coupling can create an efficient light emission channel and leads to an increase in photoluminescence (PL) and electroluminescence intensities [116–120].

SP resonance of noble metals, such as Ag and Au, occurs in the visible range. Therefore, they are most often used for SP-coupling in an InGaN/GaN QW structure. Additionally, SP resonance can be fine-tuned by controlling the size and geometry of a metal NP [121,122]. Compared with Au, Ag has a lower dissipation loss in the visible range. Therefore, it is expected to result in a larger emission enhancement [123].

Previous studies have been mainly focused on macroscopic PL enhancement through SP coupling by using Ag layers [116,117] or NPs [118–120]. For a deeper insight into the SP-coupling-enhanced PL in InGaN/GaN QW structures, in this chapter, we focus on the understanding of the LSP coupling effects of isolated Ag NPs. Confocal PL measurements are mainly employed in this study.

7.2 Samples and measurement techniques

The samples under investigation were grown in the National Taiwan University. InGaN/GaN QWs were grown using metalorganic chemical vapor deposition (MOCVD) on sapphire substrate. The sample consisted of a 2 µm GaN layer, followed by five periods of 3 nm-wide InGaN well layer and 12 nm-wide GaN barrier layer. The QW structure was covered with a 15 nm-thick GaN capping layer. Ag NPs were deposited on the top of the capping layer by using the technique of polystyrene nanosphere lithography [124]. Otherwise identical samples with (sample I) and without (sample II) Ag NPs were prepared for comparison.

The LSP resonance wavelength of the Ag NPs fabricated on the InGaN/GaN QW structure equaled ~550 nm and was matched with the effective band gap of the QWs by designing the QW parameters and the size of the Ag NPs. The average diameter of Ag NPs was 80 nm. Low surface coverage (~0.2%) enabled us to study the behavior of LSP coupling with the QWs in the vicinity of isolated NPs.

Spatially-resolved PL measurements were performed using the *WITec* microscopic system *Alpha 300* operating in confocal, scanning near field microscopy (SNOM), and atomic force microscopy (AFM) modes. A CW He-Cd laser emitting at 441.6 nm was used as the excitation source. The excitation power density was ~30 kW/cm^2. PL spectra were recorded using the spectrometer *UHTS300* equipped with a thermo-electrically cooled CCD camera. The PL measurements in confocal mode were performed in top and bottom configurations with excitation and detection from the top and bottom sides of the sample, respectively. Objectives of high numerical aperture (NA = 0.9 and NA = 0.8) ensured in-plane spatial resolution of ~240 nm and ~270 nm for the top and bottom configurations, respectively. The PL mapping image obtained in confocal mode was spatially matched with surface topography image obtained by the same microscopic system in AFM mode. The spatial resolution of the AFM measurements was ~10 nm. All the measurements were performed at room temperature.

7.3. Emission enhancement in the vicinity of large nanoparticle conglomerates

Typical spectrally-integrated PL intensity mapping images of samples I and II are shown in Figs 7.1(a) and 7.1(b), respectively. The intensity scale is the same in both images. Inhomogeneous PL intensity distribution can be seen in both samples. Such inhomogeneous distribution is due to the potential fluctuations caused by the variations of indium composition and well width [125,126]. The PL intensity is stronger in the areas, where the carriers

are localized and have a lower probability to reach nonradiative recombination centers. Though the inherently inhomogeneous PL distribution hinders the image analysis, randomly distributed bright spots, i.e., the areas exhibiting PL intensity, which exceeds the average by a factor of ~4, are clearly distinguished in sample I. No areas of such high PL intensity were observed in sample II. Spatially-integrated PL spectra averaged in the dark, intermediately bright regions, and bright spots of samples I and II are compared in Figs 7.1(c) and 7.1(d), respectively. The PL band peak position in the intermediately bright regions is only slightly redshifted in respect to that in the dark regions. This redshift can be explained by the suppressed nonradiative recombination, as

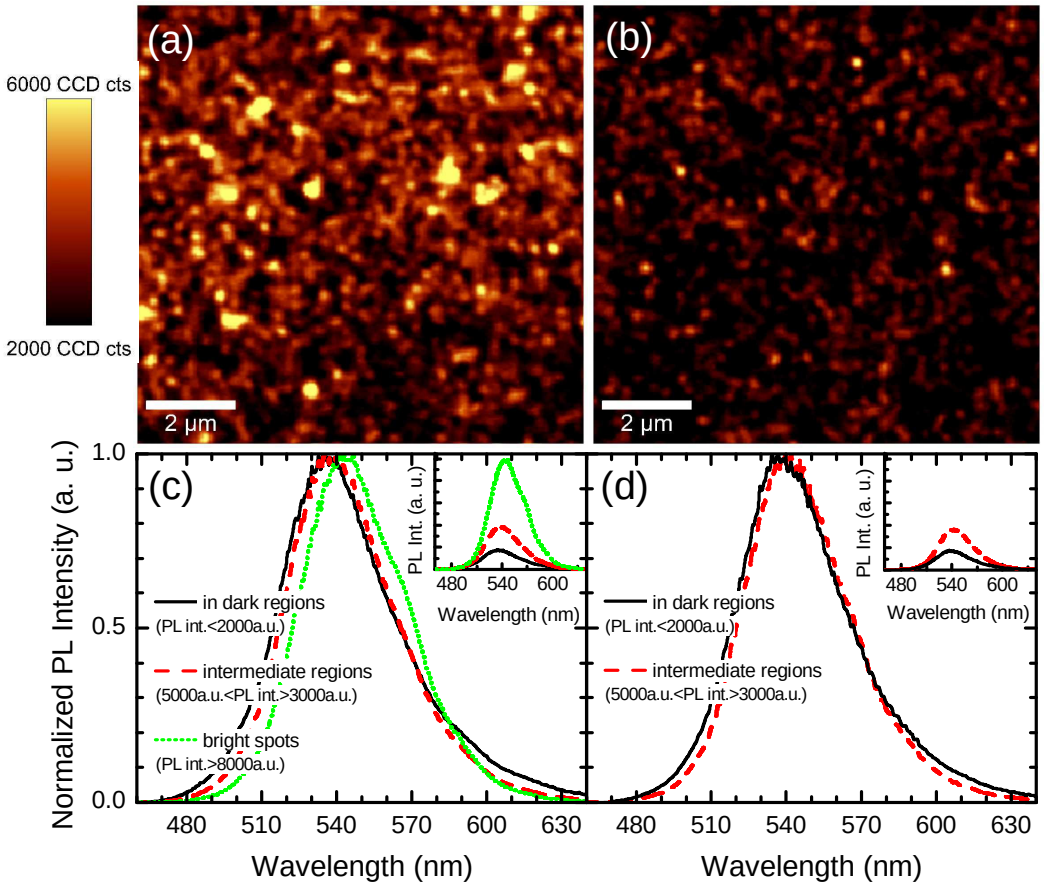

Fig. 7.1. Typical spectrally integrated spatial PL intensity distributions measured in the top configuration in an area of $10\times10\ \mu m^2$ of samples I (a) and II (b). Normalized spatially integrated PL spectra averaged in the areas of different PL intensity (indicated) of samples I (c) and II (d). [P1]

discussed above. The bright spots are observed only in sample I and exhibit the largest PL spectral redshift. This large redshift might be associated with the emission enhancement by the LSP induced on the Ag NPs. In sample I, the LSP resonance wavelength (~550 nm) is longer than that of the average PL peak of the QWs (~540 nm). Therefore, the emission on the long-wavelength side of the PL band is more strongly enhanced due to the stronger coupling of the radiating dipoles in the QWs with the LSPs on the NPs. As a result, the PL band in bright spots redshifts closer to the resonance. A redshift of the PL band peak position, though considerably smaller (3 nm), was previously observed in Ref. [124] where macroscopic PL was studied. The smaller value of the redshift can be attributed to the low surface coverage by Ag NPs: the PL from the larger part of the sample (having the major contribution to the total spatially-integrated PL intensity) is unaffected by LSP coupling. The more pronounced redshift observed in the spatially-resolved PL spectra, which are collected from sample areas near Ag NPs, evidences the PL enhancement due to Ag NPs. This conclusion is supported by the study of luminescence in the vicinity of a single Ag NP, as discussed below.

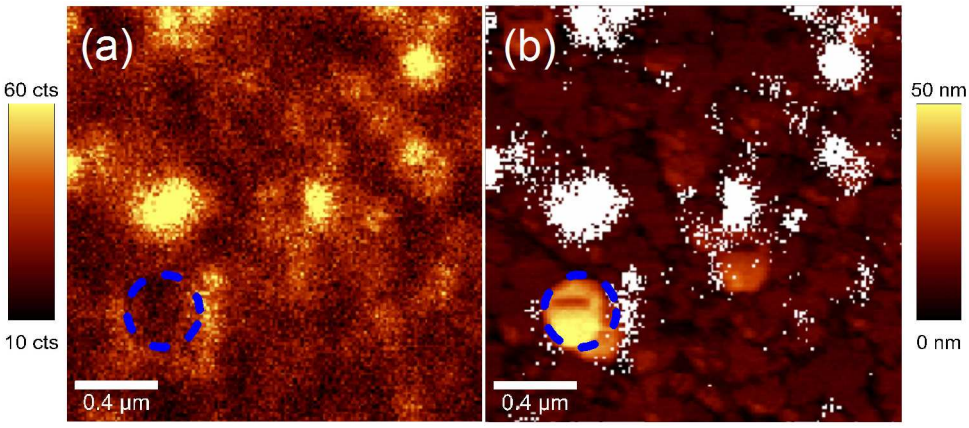

Fig. 7.2. Spectrally-integrated PL intensity mapping image (a) near Ag nanoparticle (indicated by dashed circle) and a composite image of surface topography and PL intensity of the same area (b).

The SNOM technique turned out to be inappropriate for the study of the spatial distribution of PL in the vicinity of a NP. A typical SNOM measurement is shown in Fig. 7.2. Scanning with the tip in contact with the

sample surface requires lifting the tip when the NP is approached. Therefore, the emission enhancement is counterweighed by the increasing distance between the tip and the QW layer in a hardly predictable way. Typically at the centre of the Ag NPs, lower PL intensity is observed. In addition, diameter of NPs in surface topography map is artificially broadened due to relatively large SNOM probe's tip. On the other hand, scanning with a tip fixed above the sample surface at a constant distance exceeding the NP diameter (~100 nm) provides us with a poor signal-to-noise ratio, since the near field at a distance of ~100 nm from the tip is rather weak.

To overcome the drawback of the SNOM technique, we employed confocal spectroscopy together with AFM measurements. To spatially match the images obtained in confocal and AFM modes, we used the shapes of the conglomerates of many Ag NPs. During the PL measurement in confocal mode, the conglomerate on the top of the sample surface blocks the excitation of the QWs, and a dark area is observed there. The shape of this dark area was fitted with the corresponding AFM surface topography image, so that the spatial matching of the two images can be achieved.

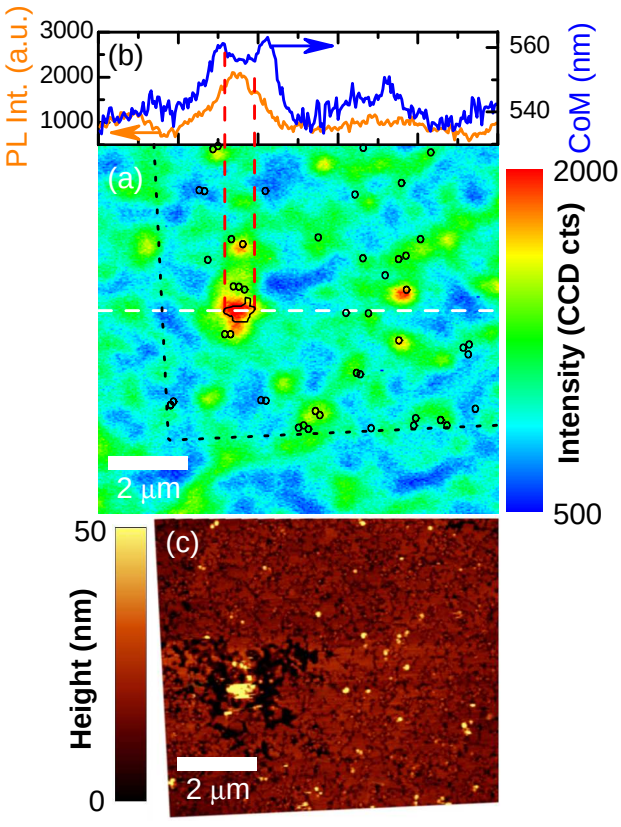

Fig. 7.3. Spectrally-integrated PL intensity mapping image in the bottom configuration of sample I with the positions of Ag NPs indicated by black circles (a) and the line-scan profiles of PL intensity and the center of mass of PL spectrum (b) along the horizontal dashed line in (a). Dotted rectangular in (a) marks area of the AFM image (c). [P1]

Figure 7.3(a) shows the PL intensity mapping image, which was recorded in the

bottom configuration around a conglomerate of Ag NPs. PL intensity enhancement is clearly observed under the conglomerate. As shown in Fig. 7.3(b), which presents the line-scan PL intensity and PL center-of-mass (CoM) wavelength along the horizontal dashed line in Fig. 7.3(a), the PL intensity increase is accompanied by a significant redshift of the spectral CoM towards the LSP resonance. This behavior has been observed before [119] and is an indication that the emission enhancement is mainly caused by SP coupling with the QWs.

7.4. Emission enhancement by a single Ag nanoparticle

The positions of single Ag NPs determined by the matching of AFM and confocal images are indicated in Fig. 7.3(a) with black circles. The actual AFM image of the corresponding area is shown in Fig. 7.3(c). Scattered Ag NPs can be clearly distinguished on a relatively flat surface. A close study of the PL intensity mapping image with superimposed NPs positions reveals that not all the areas around Ag NPs exhibit enhanced PL intensity. This behavior can be explained by the potential fluctuations, which are inherent in the InGaN/GaN QWs due to the variations of their composition and well width. Ag NPs in the regions of lower potential emit light of longer wavelengths that are closer to LSP resonance and exhibit a stronger enhancement. To confirm this conjecture, we have estimated the PL intensity and spectral CoM in an area of 200×200 nm^2 under each Ag NP. The strength of the relationship between PL intensity and spectral CoM was evaluated using the Pearson's correlation coefficient. The coefficient reflects a linear dependence between two variables and may vary between –1 and 1. A value exceeding ±0.1 is usually considered as a reliable indication of correlation or anticorrelation.

The Spearman's correlation coefficient reflecting a nonlinear correlation has also been calculated and showed the same trends as the Pearson's coefficient. Figure 7.4 shows the correlation between PL intensity and spectral CoM collected under 45 NPs and from sample I areas that are not covered by

NPs. Both data sets are collected in the bottom configuration. The solid red line in Fig. 7.4(a) demonstrates the transmission spectrum of Ag NPs. The spectrum is obtained by measuring the transmission spectrum of the sample with Ag NPs and subtracting the spectrum of the background transmission measured at the sample area not covered by Ag NPs. The minimum in this spectrum corresponds to the LSP resonance wavelength. As shown in Fig. 7.4(a), higher PL intensity is observed in the long-wavelength region of the point distribution, closer to the LSP resonance. The Pearson's correlation coefficient was evaluated to be $r = 0.52$. This value confirms a strong correlation between PL intensity and spectral CoM under Ag NPs.

Meanwhile, the Pearson's correlation coefficient calculated in the rest of the sample surface (outside the near field ranges of the Ag NPs) equals 0.08, indicating a low correlation in the regions outside the close proximity of Ag NPs [Fig. 7.4(b)]. A similar behavior ($r = 0.23$ in the close vicinity of Ag NPs and $r = 0.01$ in the rest of the surface) is observed in the top configuration.

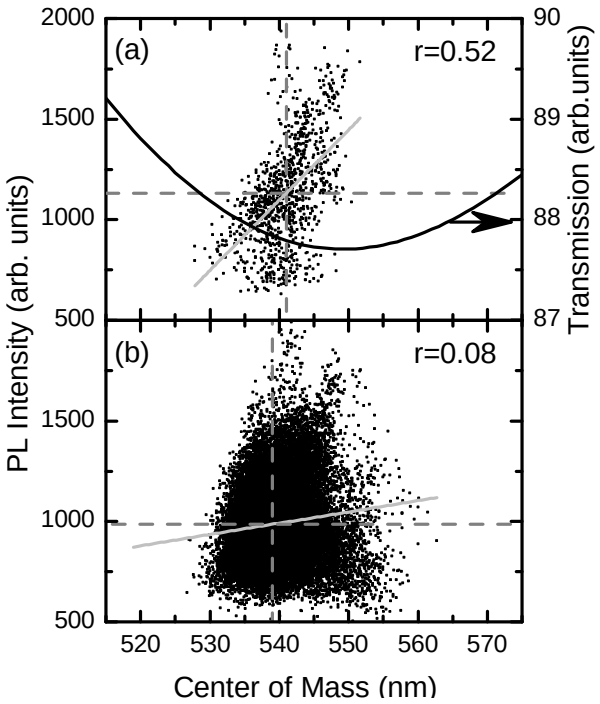

Fig. 7.4. Correlation between PL intensity and spectral center of mass under Ag NPs (a) and from areas that are not covered by NPs (b). Both data sets are collected in the bottom configuration. Vertical and horizontal dashed lines indicate the average values of PL intensity and center of mass. The solid curve shows the transmission spectrum of Ag NPs. Pearson's coefficients are indicated. [P1]

The stronger NP-induced PL enhancement in the QW areas of smaller effective band gaps is demonstrated in Fig. 7.5, where PL spectra in the vicinity of two Ag NPs are shown. The first NP is located in the region emitting light at wavelengths closer to LSP resonance (solid line), while the position of the

second NP corresponds to the off-resonance condition (dashed line), i.e., the NP is located at a position of a higher potential. The PL spectra collected in the bottom configuration, as shown in Fig. 7.5(a), are modulated by Fabry-Perot oscillations. Therefore, their peak positions are obscured. The Fabry-Perot oscillations are weaker in the top configuration, as shown in Fig. 7.5(b). A stronger PL enhancement by the Ag NP located in a lower- potential region can be clearly observed.

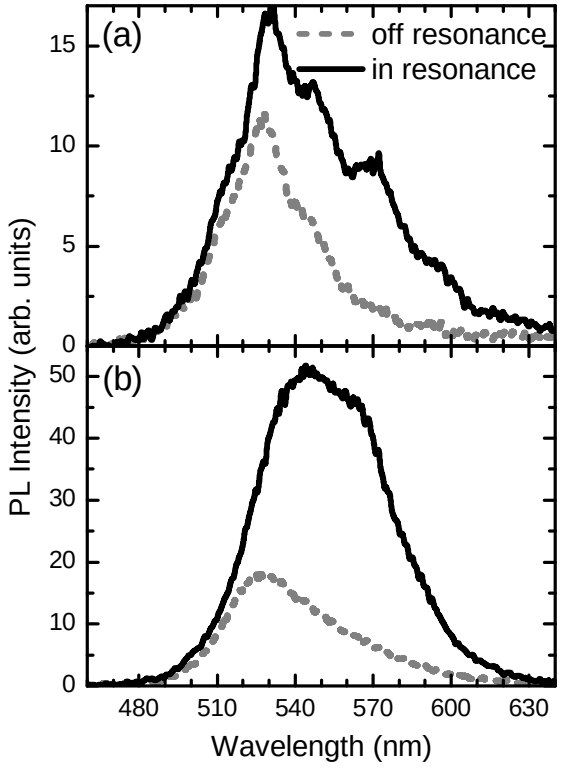

Fig. 7.5. PL spectra in the vicinity of a single Ag NP located in the region emitting light with wavelength close to the LSP resonance (solid line) and off resonance (dashed line) measured in the bottom (a) and top (b) configurations. [P1]

It is worth noting that PL intensity near an Ag NP is enhanced in the bottom configuration on average by ~15%, while the corresponding enhancement is considerably higher, up to ~46%, in the top configuration, in which Ag NPs are located between the emitting QWs and the detection system. This asymmetry in enhancement evidences the contribution of the enhancement in light extraction that is facilitated by Ag NPs. The PL enhancement through SP coupling includes the contributions of two mechanisms: the increase in radiative recombination rate [117,118] and the enhancement of the light extraction efficiency. The non-resonant light scattering by Ag NPs, which breaks the total internal reflection condition at the interface between air and GaN layer, also helps in increasing the light extraction efficiency [127]. Since the emission detected through the surface covered by Ag NPs (top configuration) is stronger than that detected in the

bottom configuration, when only the enhancement due to the increased rate of radiative recombination can be expected, the PL enhancement due to improved emission extraction plays a considerable role.

7.5. Short summary

In conclusion, enhancement of PL intensity due to coupling to localized surface plasmons in InGaN/GaN quantum wells in the vicinity of isolated Ag nanoparticles was demonstrated. The PL enhancement was strongly influenced by the inhomogeneous spatial intensity distribution caused by the potential fluctuations due to the variations of composition and width of the well. Calculations of the Pearson's coefficient for correlation between PL intensity and spectral center of mass showed that the enhancement was stronger in the sample areas emitting light at the wavelengths that better matched the resonance with the localized surface plasmons. Our study showed that the light extraction enhancement by a single silver nanoparticle was the prevailing mechanism for the increase in PL intensity.

Concluding summary

1. The transition from the initial strained layer to a subsequent relaxed layer, as the InGaN epitaxial layer is grown above the critical thickness, results in additional in-plane inhomogeneities of structural and optical properties due to formation of nanocolumn-like structures containing higher density of nonequilibrium carriers under photoexcitation. These nanocolumns have a relaxed lattice, In content as in the initial strained layer, a lower density of nonradiative recombination centers, and are surrounded by a background with relaxed lattice, higher In content, and higher defect density.

2. The defect-related emission in InGaN epilayers can be suppressed by laser annealing at power densities high enough to cause redistribution of In atoms.

3. The unintentional annealing of the active layer results in the smoothening of the potential fluctuations due to inhomogeneous indium distribution in the QWs. For thin *p*-type layers up to approximately 150 nm, the annealing improves the emission properties of the structure but becomes detrimental for thicker *p*-type layers due to the delocalization of a significant part of nonequilibrium carriers. The quantum confined Stark effect considerably influences the PL characteristics only in the structures with thin *p*-type layers and becomes unimportant due to the saturation of the internal field variation as the *p*-type layer thickness is further increased.

4. The spectral features in the dark and bright areas and dynamics of the photoluminescence characteristics under increasing excitation power density point out to an inhomogeneous distribution of nonradiative recombination centers that affects the carrier density distribution and screening of the built-in field in the QWs and leads to the nonuniform emission intensity.

5. The PL enhancement via optical dipole coupling with localized surface plasmons is strongly influenced by the potential fluctuations due to the variations of composition and width of the well. The calculations of the Pearson's coefficient for correlation between PL intensity and spectral center of mass showed that the enhancement was stronger in the sample areas emitting light at the wavelengths that better matched the resonance of the localized surface plasmons.

References

1 J. Wu and W. Walukiewicz, Superlattices Microstruct. **34**, 63 (2003).

2 J. Piprek, editor, *Nitride Semiconductor Devices* (WILEY-VCH, Weinheim, 2007).

3 I. Vurgaftman and J.R. Meyer, J. Appl. Phys. **94**, 3675 (2003).

4 J. Wu, J. Appl. Phys. **106**, 011101 (2009).

5 M. César, Y. Ke, W. Ji, H. Guo, and Z. Mi, Appl. Phys. Lett. **98**, 202107 (2011).

6 J. Wu, W. Walukiewicz, K.M. Yu, J.W. Ager, E.E. Haller, H. Lu, and W.J. Schaff, Appl. Phys. Lett. **80**, 4741 (2002).

7 E. Sakalauskas, Ö. Tuna, A. Kraus, H. Bremers, U. Rossow, C. Giesen, M. Heuken, A. Hangleiter, G. Gobsch, and R. Goldhahn, Phys. Status Solidi **249**, 485 (2012).

8 J. Wu, W. Walukiewicz, K.. Yu, J.W. Ager, S. Li, E.E. Haller, H. Lu, and W.J. Schaff, Solid State Commun. **127**, 411 (2003).

9 S.C. Jain, M. Willander, J. Narayan, and R. van Overstraeten, J. Appl. Phys. **87**, 965 (2000).

10 X. Cao, *GaN and ZnO-Based Materials and Devices* (Springer Berlin Heidelberg, Berlin, Heidelberg, 2012).

11 I. Ho and G.B. Stringfellow, Appl. Phys. Lett. **69**, 2701 (1996).

12 S. Karpov, MRS Internet J. Nitride Semicond. **3**, 16 (1998).

13 M. Hori, K. Kano, T. Yamaguchi, Y. Saito, T. Araki, Y. Nanishi, N. Teraguchi, and A. Suzuki, Phys. Status Solidi **234**, 750 (2002).

14 H.P.D. Schenk, P. de Mierry, M. Laügt, F. Omnès, M. Leroux, B. Beaumont, and P. Gibart, Appl. Phys. Lett. **75**, 2587 (1999).

15 B.N. Pantha, J. Li, J.Y. Lin, and H.X. Jiang, Appl. Phys. Lett. **93**, 182107 (2008).

16 J. Ryou, S. Member, P.D. Yoder, J. Liu, Z. Lochner, S. Member, H. Kim, S. Choi, H.J. Kim, and R.D. Dupuis, IEEE J. Sel. Top. Quantum Electron. **15**, 1080 (2009).

17 Z.C. Feng, editor, *III-Nitride Semiconductor Materials Ill-Nitride* (Imperial College Press, London, 2006).

18 M. Feneberg and K. Thonke, J. Phys. Condens. Matter **19**, 403201 (2007).

19 S. Sonderegger, E. Feltin, M. Merano, A. Crottini, J.F. Carlin, R. Sachot, B. Deveaud, N. Grandjean, and J.D. Ganière, Appl. Phys. Lett. **89**, 232109 (2006).

20 A. Hangleiter, J.S. Im, J. Off, and F. Scholz, Phys. Status Solidi **427**, 427 (1999).

21 K. Kazlauskas, G. Tamulaitis, A. Žukauskas, M.A. Khan, J.W. Yang, J. Zhang, G. Simin, M.S. Shur, and R. Gaska, Appl. Phys. Lett. **83**, 3722 (2003).

22 K. Kazlauskas, G. Tamulaitis, P. Pobedinskas, A. Žukauskas, M. Springis, C.-F. Huang, Y.-C. Cheng, and C. Yang, Phys. Rev. B **71**, 085306 (2005).

23 S. Chichibu, K. Wada, and S. Nakamura, Appl. Phys. Lett. **71**, 2346 (1997).

24 C.H. Chen, Y.F. Chen, Z.H. Lan, L.C. Chen, K.H. Chen, H.X. Jiang, and J.Y. Lin, Appl. Phys. Lett. **84**, 1480 (2004).

25 F. Bertram, S. Srinivasan, L. Geng, and F.A. Ponce, Phys. Status Solidi **39**, 35 (2001).

26 Y. Narukawa, Y. Kawakami, M. Funato, S. Fujita, and S. Fujita, Appl. Phys. Lett. **70**, 981 (2001).

27 P. Ruterana, S. Kret, A. Vivet, G. Maciejewski, and P. Dluzewski, J. Appl. Phys. **91**, 8979 (2002).

28 D. Gerthsen and O. Scho, Phys. Status Solidi **145**, 145 (2000).

29 T.M. Smeeton, M.J. Kappers, J.S. Barnard, M.E. Vickers, and C.J. Humphreys, Appl. Phys. Lett. **83**, 5419 (2003).

30 S.J. Henley and D. Cherns, J. Appl. Phys. **93**, 3934 (2003).

31 J.K. Son, S.N. Lee, T. Sakong, H.S. Paek, O. Nam, Y. Park, J.S. Hwang, J.Y. Kim, and Y.H. Cho, J. Cryst. Growth **287**, 558 (2006).

32 K. Okamoto, J. Choi, Y. Kawakami, M. Terazima, T. Mukai, and S. Fujita, Jpn. J. Appl. Phys. **43**, 839 (2004).

33 T.S. Ko, T.C. Lu, T.C. Wang, J.R. Chen, R.C. Gao, M.H. Lo, H.C. Kuo, S.C. Wang, and J.L. Shen, J. Appl. Phys. **104**, 093106 (2008).

34 S. De, A. Layek, S. Bhattacharya, D. Kumar Das, A. Kadir, A. Bhattacharya, S. Dhar, and A. Chowdhury, Appl. Phys. Lett. **101**, 121919 (2012).

35 K. Okamoto, A. Kaneta, Y. Kawakami, S. Fujita, J. Choi, M. Terazima, and T. Mukai, J. Appl. Phys. **98**, 064503 (2005).

36 A. Kaneta, K. Okamoto, Y. Kawakami, S. Fujita, G. Marutsuki, Y. Narukawa, and T. Mukai, Appl. Phys. Lett. **81**, 4353 (2002).

37 G. Marutsuki, Y. Narukawa, T. Mitani, T. Mukai, G. Shinomita, A. Kaneta, Y. Kawakami, and S. Fujita, Phys. Status Solidi **116**, 110 (2002).

38 A. Kaneta, D. Yamada, G. Marutsuki, Y. Narukawa, T. Mukai, and Y. Kawakami, Phys. Status Solidi **2**, 2728 (2005).

39 A. Kaneta, G. Marutsuki, K. Okamoto, and Y. Kawakami, Phys. Status Solidi **156**, 153 (2001).

40 A. Kaneta, M. Funato, and Y. Kawakami, Phys. Rev. B **78**, 125317 (2008).

41 S. Mahanty, M. Hao, T. Sugahara, R. Fareed, Y. Morishima, Y. Naoi, T. Wang, and S. Sakai, Mater. Lett. **41**, 67 (1999).

42 I. Gan, Q. Wells, M.S. Jeong, D. Ko, J. Lee, Y. Kim, and J.O. White, J. Korean Phys. Soc. **47**, 209 (2005).

43 M.S. Jeong, Y.-W. Kim, J.O. White, E.-K. Suh, M.G. Cheong, C.S. Kim, C.-H. Hong, and H.J. Lee, Appl. Phys. Lett. **79**, 3440 (2001).

44 M. Reshchikov and H. Morkoç, J. Appl. Phys. **97**, 061301 (2005).

45 F. Hitzel, G. Klewer, S. Lahmann, U. Rossow, and a. Hangleiter, Phys. Rev. B **72**, 081309 (2005).

46 Y. Nan and Z.L. Wang, editors, *Handbook of Microscopy for Nanotechnology* (Kluwer Academic Publishers, New York, NY, 2005).

47 G. Tamulaitis, Mater. Sci. **17**, 343 (2011).

48 A. R. Clarke and C.N. Eberhardt, *Microscopy Techniques for Materials Science* (Woodhead Publishing Limited, Cambridge, 2002).

49 B. Bhushan, H. Fuchs, and M. Tomitori, editors, *Applied Scanning Probe Methods VIII* (Springer, New York, NY, 2008).

50 S. Pereira, M.R. Correia, E. Pereira, C. Trager-Cowan, F. Sweeney, K.P. O'Donnell, E. Alves, N. Franco, and A.D. Sequeira, Appl. Phys. Lett. **81**, 1207 (2002).

51 B.R. Jampana, C.R. Weiland, R.L. Opila, I.T. Ferguson, and C.B. Honsberg, Thin Solid Films **520**, 6807 (2012).

52 C. Parker and J. Roberts, Appl. Phys. Lett. **77**, 4121 (1999).

53 M. Leyer, J. Stellmach, C. Meissner, M. Pristovsek, and M. Kneissl, J. Cryst. Growth **310**, 4913 (2008).

54 S. Pereira, M.R. Correia, E. Pereira, K.P. O'Donnell, E. Alves, A.D. Sequeira, and N. Franco, Appl. Phys. Lett. **79**, 1432 (2001).

55 S.M.D.S. Pereira, K.P. O'Donnell, and E. Jorge da Costa Alves, Adv. Funct. Mater. **17**, 37 (2007).

56 B. Wilsch, U. Jahn, B. Jenichen, J. Lähnemann, H.T. Grahn, H. Wang, and H. Yang, Appl. Phys. Lett. **102**, 052109 (2013).

57 Z. Liliental-Weber, M. Benamara, J. Washburn, J.Z. Domagala, J. Bak-Misiuk, E.L. Piner, J.C. Roberts, and S.M. Bedair, J. Electron. Mater. **30**, 439 (2001).

58 M.J. Reed, N. Carolina, C.A. Parker, J.C. Roberts, and S.M. Bedair, Appl. Phys. Lett. **77**, 4121 (2000).

59 M.A. Moram and M.E. Vickers, Reports Prog. Phys. **72**, 036502 (2009).

60 R. Liu, J. Mei, S. Srinivasan, F.A. Ponce, H. Omiya, Y. Narukawa, and T. Mukai, Appl. Phys. Lett. **89**, 201911 (2006).

61 S. Srinivasan, L. Geng, R. Liu, F.A. Ponce, Y. Narukawa, and S. Tanaka, Appl. Phys. Lett. **83**, 5187 (2003).

62 J.R. Jinschek, R. Erni, N.F. Gardner, A.Y. Kim, and C. Kisielowski, Solid State Commun. **137**, 230 (2006).

63 M.D. McCluskey, C.G. Van de Walle, C.P. Master, L.T. Romano, and N.M. Johnson, Appl. Phys. Lett. **72**, 2725 (1998).

64 A.F. Wright, K. Leung, and M. van Schilfgaarde, Appl. Phys. Lett. **78**, 189 (2001).

65 Y. Kawaguchi, M. Shimizu, M. Yamaguchi, K. Hiramatsu, N. Sawaki, W. Taki, H. Tsuda, N. Kuwano, K. Oki, T. Zheleva, and R.F. Davis, J. Cryst. Growth **190**, 24 (1998).

66 N. Grandjean, J. Massies, M. Leroux, and P. De Mierry, Appl. Phys. Lett. **72**, 3190 (1998).

67 C. Manz, M. Kunzer, H. Obloh, a. Ramakrishnan, and U. Kaufmann, Appl. Phys. Lett. **74**, 3993 (1999).

68 W. Lü, J. Appl. Phys. **95**, 4362 (2004).

69 S.-W. Feng, E.-C. Lin, T.-Y. Tang, Y.-C. Cheng, H.-C. Wang, C.C. Yang, K.-J. Ma, C.-H. Shen, L.C. Chen, K.H. Kim, J.Y. Lin, and H.X. Jiang, Appl. Phys. Lett. **83**, 3906 (2003).

70 M. Godlewski, E.M. Goldys, G. Pozina, B. Monemar, K. Pakula, J.M. Baranowski, P. Prystawko, and M. Leszczynski, **310**, 102 (2001).

71 J. Mickevičius, R. Aleksiejūnas, M.S. Shur, S. Sakalauskas, G. Tamulaitis, Q. Fareed, and R. Gaska, Appl. Phys. Lett. **86**, 041910 (2005).

72 C.B. Soh, S.J. Chua, S. Tripathy, W. Liu, and D.Z. Chi, J. Phys. Condens. Matter **17**, 729 (2005).

73 J.C. Zolper, M.H. Crawford, and A.J. Howard, **68**, 200 (2001).

74 C.-C. Chen, K.-L. Hsieh, G.-C. Chi, C.-C. Chuo, J.-I. Chyi, and C.-A. Chang, Solid. State. Electron. **46**, 1123 (2002).

75 N.K. van der Laak, R.A. Oliver, M.J. Kappers, and C.J. Humphreys, J. Appl. Phys. **102**, 013513 (2007).

76 P.R. Chalker, D. Morrice, T.B. Joyce, T.C.Q. Noakes, P. Bailey, and L. Considine, Diam. Relat. Mater. **9**, 520 (2000).

77 G.T. Thaler, D.D. Koleske, S.R. Lee, K.H.A. Bogart, and M.H. Crawford, J. Cryst. Growth **312**, 1817 (2010).

78 M.H. Zaldívar, P. Fernández, J. Piqueras, and J. Solís, J. Appl. Phys. **85**, 1120 (1999).

79 C. Chuo, C. Lee, T. Nee, and J. Chyi, Appl. Phys. Lett. **76**, 3902 (2000).

80 C.-C. Chuo, M.N. Chang, F.-M. Pan, C.-M. Lee, and J.-I. Chyi, Appl. Phys. Lett. **80**, 1138 (2002).

81 Y.-S. Lin, K.-J. Ma, C.C. Yang, and T.E. Weirich, J. Cryst. Growth **242**, 35 (2002).

82 Y.-Y. Chung, Y.-S. Lin, S.-W. Feng, Y.-C. Cheng, E.-C. Lin, C.C. Yang, K.-J. Ma, C. Hsu, H.-W. Chuang, C.-T. Kuo, and J.-S. Tsang, J. Appl. Phys. **93**, 9693 (2003).

83 S.-W. Feng, T.-Y. Tang, Y.-C. Lu, S.-J. Liu, E.-C. Lin, K.-J. Ma, C.-H. Shen, L.C. Chen, K.H. Kim, J.Y. Lin, and H.X. Jiang, J. Appl. Phys. **95**, 5388 (2004).

84 H.F. Liu, W. Liu, A.M. Yong, X.H. Zhang, S.J. Chua, and D.Z. Chi, J. Appl. Phys. **110**, 063505 (2011).

85 Q.L. Diode, C. Liao, C. Chen, H. Chen, K. Chen, W. Chung, W. Chang, J.-J. Huang, Y.-F. Yao, Kiang, Yean-Woei, and C.-C. Yang, IEEE Photonics Technol. Lett. **23**, 1757 (2011).

86 C.-Y. Chen, C. Hsieh, C.-H. Liao, W.-L. Chung, H.-T. Chen, W. Cao, W.-M. Chang, H.-S. Chen, Y.-F. Yao, S.-Y. Ting, Y.-W. Kiang, C.C. Yang, and X. Hu, Opt. Express **20**, 11321 (2012).

87 C. Hums, T. Finger, T. Hempel, J. Christen, A. Dadgar, A. Hoffmann, and A. Krost, J. Appl. Phys. **101**, 033113 (2007).

88 Y. Kangawa, N. Kawaguchi, Y. Kumagai, and A. Koukitu, J. Cryst. Growth **272**, 444 (2004).

89 A.G. Bhuiyan, T. Tanaka, K. Kasashima, A. Hashimoto, and A. Yamamoto, Jpn. J. Appl. Phys. **42**, 7284 (2003).

90 Y. Guo, X.L. Liu, H.P. Song, A.L. Yang, X.Q. Xu, G.L. Zheng, H.Y. Wei, S.Y. Yang, Q.S. Zhu, and Z.G. Wang, Appl. Surf. Sci. **256**, 3352 (2010).

91 A. Medvid, Defect Diffus. Forum **210-212**, 89 (2002).

92 V. Liuolia, A. Pinos, S. Marcinkevičius, Y.D. Lin, H. Ohta, S.P. DenBaars, and S. Nakamura, Appl. Phys. Lett. **97**, 151106 (2010).

93 A. Pinos, V. Liuolia, S. Marcinkevičius, J. Yang, R. Gaska, and M.S. Shur, J. Appl. Phys. **109**, 113516 (2011).

94 M. Leroux, N. Grandjean, J. Massies, B. Gil, P. Lefebvre, M. Ii, C. Courrier, M. Cedex, and P. Bigenwald, Phys. Rev. B **60**, 1496 (1999).

95 S.F. Chichibu, A. Uedono, T. Onuma, B. a Haskell, A. Chakraborty, T. Koyama, P.T. Fini, S. Keller, S.P. Denbaars, J.S. Speck, U.K. Mishra, S. Nakamura, S. Yamaguchi, S. Kamiyama, H. Amano, I. Akasaki, J. Han, and T. Sota, Nat. Mater. **5**, 810 (2006).

96 D. Cherns, S.J. Henley, and F.A. Ponce, Appl. Phys. Lett. **78**, 2691 (2001).

97 J.C. Brooksby, J. Mei, and F.A. Ponce, Appl. Phys. Lett. **90**, 231901 (2007).

98 H. Gotoh, T. Akasaka, T. Tawara, Y. Kobayashi, T. Makimoto, and H. Nakano, Solid State Commun. **138**, 590 (2006).

99 E. Oh, H. Park, C. Sone, O. Nam, Y. Park, and T. Kim, Solid State Commun. **113**, 461 (2000).

100 K.P. O'Donnell, C.T. Cowan, S. Pereira, and A. Bangura, Phys. Status Solidi **216**, 157 (1999).

101 C. Vierheilig, H. Braun, U.T. Schwarz, W. Wegscheider, E. Baur, U. Strauß, and V. Härle, Phys. Status Solidi **4**, 2362 (2007).

102 D.M. Graham, A. Soltani-Vala, P. Dawson, M.J. Godfrey, T.M. Smeeton, J.S. Barnard, M.J. Kappers, C.J. Humphreys, and E.J. Thrush, J. Appl. Phys. **97**, 103508 (2005).

103 F. Hitzel, A. Hangleiter, S. Bader, and H. Lugauer, Phys. Status Solidi **228**, 407 (2001).

104 J. Narayan, H. Wang, J. Ye, S.-J. Hon, K. Fox, J.C. Chen, H.K. Choi, and J.C.C. Fan, Appl. Phys. Lett. **81**, 841 (2002).

105 S.-Y. Kwon, H.J. Kim, E. Yoon, Y. Jang, K.-J. Yee, D. Lee, S.-H. Park, D.-Y. Park, H. Cheong, F. Rol, and L.S. Dang, J. Appl. Phys. **103**, 063509 (2008).

106 A. Hangleiter, F. Hitzel, C. Netzel, D. Fuhrmann, U. Rossow, G. Ade, and P. Hinze, Phys. Rev. Lett. **95**, 127402 (2005).

107 L. Bellaiche, T. Mattila, L.-W. Wang, S.-H. Wei, and a. Zunger, Appl. Phys. Lett. **74**, 1842 (1999).

108 P. Riblet, H. Hirayama, A. Kinoshita, A. Hirata, T. Sugano, and Y. Aoyagi, Appl. Phys. Lett. **75**, 2241 (1999).

109 U. Ozgur, H. Liu, X. Li, X. Ni, and H. Morkoc, Proc. IEEE **98**, 1180 (2010).

110 V. Fiorentini, F. Bernardini, F. Della Sala, A. Di Carlo, P. Lugli, and T. Vergata, **60**, 8849 (1999).

111 G.E. Dialynas, G. Deligeorgis, M. Zervos, and N.T. Pelekanos, J. Appl. Phys. **104**, 113101 (2008).

112 Y.-L. Li, Y.-R. Huang, and Y.-H. Lai, Appl. Phys. Lett. **91**, 181113 (2007).

113 S.F. Chichibu, H. Marchand, M.S. Minsky, S. Keller, P.T. Fini, and J.P. Ibbetson, **74**, 1460 (1999).

114 C.-H. Lin, C.-Y. Chen, C.-H. Liao, C. Hsieh, Y.-W. Kiang, and C.-C. Yang, IEEE Photonics Technol. Lett. **23**, 654 (2011).

115 C. Sasaoka, H. Sunakawa, A. Kimura, M. Nido, A. Usui, and A. Sakai, **190**, 61 (1998).

116 A. Neogi, C.-W. Lee, H. Everitt, T. Kuroda, A. Tackeuchi, and E. Yablonovitch, Phys. Rev. B **66**, 153305 (2002).

117 K. Okamoto, I. Niki, A. Scherer, Y. Narukawa, T. Mukai, and Y. Kawakami, Appl. Phys. Lett. **87**, 071102 (2005).

118 M.-K. Kwon, J.-Y. Kim, B.-H. Kim, I.-K. Park, C.-Y. Cho, C.C. Byeon, and S.-J. Park, Adv. Mater. **20**, 1253 (2008).

119 D.-M. Yeh, C.-F. Huang, C.-Y. Chen, Y.-C. Lu, and C.C. Yang, Nanotechnology **19**, 345201 (2008).

120 J. Henson, J.C. Heckel, E. Dimakis, J. Abell, A. Bhattacharyya, G. Chumanov, T.D. Moustakas, and R. Paiella, Appl. Phys. Lett. **95**, 151109 (2009).

121 J. Henson, J. DiMaria, and R. Paiella, J. Appl. Phys. **106**, 093111 (2009).

122 J. Henson, E. Dimakis, J. Dimaria, R. Li, S. Minissale, L.D. Negro, T.D. Moustakas, and R. Paiella, **18**, 4721 (2010).

123 P.R. West, S. Ishii, G.V. Naik, N.K. Emani, V.M. Shalaev, and A. Boltasseva, Laser Photon. Rev. **4**, 795 (2010).

124 C.-W. Huang, H.-Y. Tseng, C.-Y. Chen, C.-H. Liao, C. Hsieh, K.-Y. Chen, H.-Y. Lin, H.-S. Chen, Y.-L. Jung, Y.-W. Kiang, and C.C. Yang, Nanotechnology **22**, 475201 (2011).

125 Y. Yamada, T. Saito, N. Kato, E. Kobayashi, T. Taguchi, H. Kudo, and H. Okagawa, Phys. Rev. B **80**, 195202 (2009).

126 Y.-S. Lin, K.-J. Ma, C. Hsu, S.-W. Feng, Y.-C. Cheng, C.-C. Liao, C.C. Yang, C.-C. Chou, C.-M. Lee, and J.-I. Chyi, Appl. Phys. Lett. **77**, 2988 (2000).

127 J.-H. Sung, B.-S. Kim, C.-H. Choi, M.-W. Lee, S.-G. Lee, S.-G. Park, E.-H. Lee, and O. Beom-Hoan, Microelectron. Eng. **86**, 1120 (2009).